2007

Improving Pulsar Timing through Interstellar Scatter Correction

Daniel Hemberger
Oberlin College

Repository Citation

Hemberger, Daniel, "Improving Pulsar Timing through Interstellar Scatter Correction" (2007). *Honors Papers*. 450.
https://digitalcommons.oberlin.edu/honors/450

Improving Pulsar Timing through Interstellar Scatter Correction

DANIEL A. HEMBERGER
APRIL 2007

An Honors thesis presented to the
Department of Physics & Astronomy
Oberlin College

April 5, 2007

Contents

List of Figures

Acknowledgements

An invaluable tool in our research was a wave-propagation code that we received from Bill Coles (UCSD) and collaborators. Jon Myers (Oberlin College, 2006) parallelized the code for use on the Oberlin supercomputer and Nate Daniels (Oberlin College) was our heroic supercomputer technician. I thank them all for their contributions to this project.

“People have calculated the ACFs of Dynamic Spectra for hundreds, if not thousands, of years.” There is only one man in the world who can and will jest about interstellar scintillations. This man has whisked me across the globe, from Arecibo in Puerto Rico to the VLA in New Mexico to the University of Leiden in the Netherlands. He has helped me mature scientifically and personally, and has done more than anyone could ask to prepare me for the next step of my academic career. This man is Dan Stinebring, a great advisor and friend, and I owe him an infinite debt of gratitude.

Dedication

This thesis is dedicated to Uncle Bo. Though he never had the scientific opportunities that I do, his insatiable curiosity never diminished, and his unparalleled enthusiasm was always refreshing and inspiring. May we all be as innocent and earnest as Uncle Bo in our pursuit of knowledge.

Eschew obfuscation.

Chapter 1

Introduction

1.1 Pulsars and the Interstellar Medium

Pulsars were once stars more massive than our Sun, supported by thermal pressure fueled by nuclear interactions in their cores. During the tumult of a supernova, their cores collapsed and gravity overcame electromagnetic repulsion and electron degeneracy pressure. The electrons were smashed into the protons, creating a neutron superfluid. There are so many neutrons in such a small volume that pulsars are held from the brink of collapse into a black hole by neutron degeneracy pressure. These unfathomably dense stars are about the size of Cleveland and have masses not much greater than our Sun, yet some perform a full rotation in about a millisecond.

Fascination is not the only reason astrophysicists study pulsars; they are *useful* too. Pulsars emit a characteristic "lighthouse" beam with extraordinary periodicity. This beam is received by radio telescopes as pulses of power and can reveal a wealth of information about pulsars and fundamental processes in the universe.

No matter how well a telescope can resolve an area of the sky, there are two intrinsic reasons why the received signal is distorted: dispersion and scattering. If the signal traveled through vacuum, there would be no distortion. But interstellar space is filled with gas, dust, and free electrons. These constitute the interstellar medium (ISM), which is an important component of our galaxy, but a fundamental hindrance in radio frequency observations.

Free electrons slow the propagation of electromagnetic waves, delaying most those with low frequencies. This is dispersion. Its mathematical effect is a convolution of the detected signal with a chirp function, which can be undone with great accuracy if the column density of electrons between the telescope and the pulsar is known[1]. One can take the Fourier Transform of the detected signal and the chirp function and then take the inverse Fourier Transform of their quotient. This deconvolution technique yields a coherently dedispersed signal.

Dedispersion is simple because dispersion is deterministic, but it is still a challenge to determine the column density of electrons, also known as *Dispersion Measure* (DM),

$$\mathrm{DM} = \int n_e \, d\ell. \tag{1.1}$$

We must also grapple with scattering, which causes interference between radio waves that have taken distinct paths through the ISM. The effect of scattering is a convolution of the intrinsic pulsar signal, $i(t)$, with the impulse response of the ISM[2], $h(t)$,

$$i(t) \overset{\text{ISM}}{\longrightarrow} i(t) * h(t). \tag{1.2}$$

One difficulty with descattering lies in the stochastic nature of scattering. Since scattering is strongest at low frequencies, astronomers tend to observe at higher radio frequencies when they need to limit its effects. Such is the case with high-precision pulsar timing. There is a tradeoff at high frequencies, though: the effects of scattering are limited, but signal strength, which falls rapidly as frequency increases, is sacrificed. Another difficulty is that the impulse response is not an observable. What we can measure is its autocorrelation function, $R_h(t)$,

$$R_h(t) = \int h(t')h(t'+t) \, dt'. \tag{1.3}$$

This quantity is the staple of my thesis and will be used throughout.

Because a pulsar is essentially a point source, interference caused by scattering in the turbulent ISM modulates the signal intensity, which is an effect called *scintillation.* If the turbulence can be characterized by a Kolmogorov distribution of inhomogeneities in the ISM, then scintillation produces parabolic arcs in the power spectrum of a pulsar's dynamic spectrum[3]. Sources of pulse power (called "arclets") have recently been discovered along these arcs and are thought to arise from scattering off compact (AU-sized), overdense structures in the ISM[4]. Arclet power persists to large time delays and is not predicted in conventional models of the ISM.

Pulsars are high-velocity objects[a], so they rapidly probe the spatial structure of the ISM as they move across the sky. This changes the column density of electrons (the DM) as well as the volume of inhomogeneities that contributes to scattering. The result is a *time-variable delay* of the pulsar signal from propagation through the ISM.

1.2 Pulsar Timing and Gravitational Waves

Gravitational-wave (GW) astronomy promises to usher in a new era of scientific understanding. Until recently, we have been content to see the world with electromagnetic eyes. Our discontent emerged when we discovered that some wonders in the universe reveal themselves only to those who see with gravitational eyes. GW detection is nothing like the discovery

---

[a] The median pulsar velocity is 350 km/s[5].

of a new electromagnetic band. The most cataclysmic events in the history of the universe are linked to us gravitationally, but obscured electromagnetically – the Big Bang, inflation, the merger of supermassive black holes. An undiscovered universe waits to be found. All we need to do is open our gravitational eyes.

Gravitational radiation is analogous to dipole radiation in electromagnetism, except GWs are quadrupolar to leading order[6]. Their quadrupole nature and the weakness of the gravitational interaction indicate that large masses with relativistic accelerations are required to produce them. Much like pulsars, it is unlikely that GWs will ever be studied in a laboratory.

However, pulsars can be used as a remote laboratory for studying GWs because they are extremely stable clocks. They have already provided evidence for the existence of GWs through the orbital decay of binary pulsar systems, and they have been instrumental in the most thorough tests of General Relativity to date[7;8].

A plane GW can change the propagation time of a pulsar signal by perturbing the spacetime of the pulsar at the time of emission and the earth at the time of reception. These perturbations will be correlated between different pulsars, and a set of pulsars used to detect this correlation is called a Pulsar Timing Array (PTA) – a high-precision interferometric GW detector built for us by nature! PTAs uniquely detect nanoHertz GWs, complementing the higher frequency detectors (LIGO, LISA, etc.).

While not yet sensitive enough to detect an individual GW, PTAs are within range to detect a stochastic GW background produced primarily by massive black hole (BH) interactions in galactic mergers. A detection would allow us to better understand the galactic merger history – which defines the morphology of present-day galaxies – and also limit the efficiency of BH mergers and the ubiquity of BHs in low-redshift galaxies[9]. Competing theories of gravity can be tested by the GW backgrounds they predict from BH mergers.

Many sources of random and systematic error are corrected for in pulsar timing, but scattering in the ISM is not. However, pulsar timing is approaching a level of precision where interstellar scattering is significant, and there is evidence that the effect may be bigger than previously thought. For example, the substantive effect of arclets on pulsar timing is overlooked.

To see how scattering manifests itself in a PTA, we must first understand the timing procedure. The observable in a pulsar timing observation is the pulse intensity, $I \propto |E|^2$. A pulse profile is obtained by folding about five minutes of intensity data over the pulsar's period, which must be carefully adjusted for the motion of the observatory relative to an inertial reference frame. Each epoch is assigned a time of arrival (TOA), which is calculated from the lag of maximum cross-correlation between the pulse profile and a standard profile (an ideal and static representation of the pulse profile). The topocentric TOA must then be converted into a proper time of emission at the pulsar, correcting for systematic effects by a least-squares fitting procedure[10]. The ultimate quantity, a set of timing residuals Δt_j, is derived by differencing a set of proper emission times, t_j, and a fiducial emission period, T.

$$\Delta t_j = t_j - j\,T \tag{1.4}$$

Aptly named, it comprises the residual error of the timing procedure.

Multi-year residuals of a PTA are searched for correlated nanoHertz signals. The correlation and accompanying significance establish an upper bound for or detection of a stochastic GW background[11]. Interstellar scattering reduces the correlation by introducing uncorrelated delays from pulsar to pulsar and epoch to epoch. The focus of my research is to identify and correct for this effect so as to improve the sensitivity of PTAs to GW perturbations.

1.3 Project Summary and Results

Though pulsar timing has confirmed the existence of gravitational waves[10], no technique has directly detected them. Jenet *et al.*[11] state the requirements for the Parkes Pulsar Timing Array (PPTA) to make a significant detection of the stochastic gravitational wave background within five years. By employing the scintillation information in observations for each pulsar at every epoch, I believe interstellar scattering, an underestimated source of timing noise, can be corrected enough for the PPTA to meet these requirements. The improved detection threshold will help answer important questions about black hole mergers, galaxy evolution, and gravitation.

I have approached this problem in three different ways, using the tools of observational, theoretical, and computational physics:

1) an observational study of pulsar scintillation data,

2) a primarily analytic study of the effect of scattering on pulse time of arrivals, and

3) a simulation of wave propagation through random, dispersive media.

The results are summarized immediately below, but are expounded in Chapters 3, 4, and 5 respectively. In Chapter 2, I provide background information for the three results chapters.

The convolution of a pulsar's intrinsic pulse with the impulse response of the ISM perturbs the pulse center by introducing a temporal shift and a broadening. These effects fluctuate between observations because the pulsar rapidly probes the spatial structure of the ISM due to its high velocity. The spatial variation in the ISM becomes a time-variability in the pulse power, especially as arclets translate along the scintillation arc[4]. Therefore, the TOA of the pulse will also vary in a way that can be approximated with the scintillation information in the power spectrum of the pulsar's dynamic spectrum.

In Chapter 3, the variability of delay is quantified for the pulsar PSR B1737+13. Careful attention is paid to noise in the data because the delay is heavily influenced by low-level power. Arclets are shown to be the major low-level contributor to the delay. Temporal partitioning of the observations and multi-frequency analysis allows us to comment on the robustness and uncertainty in our technique. The measurements are intended to be used as a scatter-correction for pulsar timing residuals.

We must justify our measurements as scattering delays. To do so, in Chapter 4 we construct a simplified model of the impulse response, parameterized by a width τ and an offset t_0, to determine precisely how scattering in this $t_0\tau$ Model affects pulsar timing. In any observationally relevant regime, the induced delay is given by the centroid of the impulse response, $\Gamma_h = t_0 + \tau$. Furthermore, if the impulse response is narrow enough, its effect on the pulse is merely a shift in time by the centroid. Without any broadening, time-domain efforts to detect this delay are impotent and our spectral analysis becomes crucial.

The observational method cannot determine a t_0 component of the impulse response centroid, and the $t_0\tau$ Model does not constrain the behavior of t_0. To account for this, we must either find a way to remove the offset or determine some statistical properties of t_0 to correct the timing residuals with the information that *is* available. Thus the wave-propagation simulation is used in Chapter 5 to bridge the gap between the observationally determined delay and the $t_0\tau$ Model. Dedispersing the simulation data removes an offset t_0 (or reduces it to a level where it could be corrected for statistically). With this last piece in place, we are justified in using our observational method to determine an interstellar delay that can be used to correct timing residuals.

I believe this correction can benefit PTAs. Jenet *et al.*[11] show that a PTA of 40 pulsars with residuals smaller than 100 ns could make a direct detection of the predicted GW background within five years. The PPTA is striving to meet these constraints, but does not yet have sufficient timing precision. This research has determined that scattering delay can vary on the microsecond level, so a scatter correction will be necessary to achieve 100 ns residuals for many pulsars. If dynamic spectra are obtained during each timing observation, then scattering delays can be calculated with the algorithm presented in §3.1 and subtracted from the timing residuals. Because the uncorrected residuals are comparable in magnitude to the scattering delay variations, the correction could reduce the residuals to below 100 ns, thus increasing the fractional contribution of the GW background to a level the PPTA can detect.

Whether elucidating astrophysical processes, supplementing electromagnetic wave observations, or probing the early universe, GW detections would prove observationally indispensable and revolutionary in their scientific consequences.

Chapter 2

Background

Propagation effects have been an important topic in the study of pulsars[1;12]. At the most rigorous level they have prompted the simulation of wave propagation in random dispersive media[13–15]. There has been discussion about interstellar optics[16], the impulse response of the ISM[17], and various time domain effects[18].

Because scintillation theory[19;20] and observation[21–23] are so inextricably entwined with the structure of the ISM[24–30], the analysis techniques have become quite advanced. The maturation of this field can be seen in the analysis of the power spectrum of the pulsar's dynamic spectrum[2;3;31–35].

Great strides in the understanding of the ISM have improved the use of pulsars as extremely stable clocks[10;36;37]. As the creative application of pulsars burgeoned, it was realized that gravitational wave backgrounds[9] could be detected using pulsar timing arrays[11;38–41] in a complementary regime to the man-made gravitational wave detectors. However, timing noise is a limiting factor, and recent analysis has shown that time-variable ISM propagation delays are emerging as a major problem[42]. Much of the success of pulsar timing has relied on the analysis of dispersive propagation effects[42–46], but analyses of scattering[47–49] have yet to be used significantly by the pulsar timing community.

2.1 Scintillation in the ISM

Dispersion Measure (DM) is the integrated electron density, n_e, along the line of sight between two points separated by a distance D,

$$\mathrm{DM} = \int_0^D n_e \, d\ell. \tag{2.1}$$

The effects of DM can be approximated by rearranging the distribution of electrons along the line of sight so that all the electrons are localized in a two-dimensional screen[49] as in Figure 2.1. Pulsars are high-velocity objects, so as they move across the sky, they rapidly sample the spatial structure of the screen, which is essentially frozen because the timescale for variation in the ISM is so long[a].

Refraction in the screen allows rays propagating from the pulsar in multiple directions to reach the Earth. The length scale of the screen at which refracted rays focus as the Earth is called the refractive scale, s_r. It is given by

$$s_r \approx D_s \theta_d, \tag{2.2}$$

where D_s is the distance from the Earth to the screen and θ_d is the angle that subtends the refractive scale (see Fig. 2.1). Schematically, the screen acts like a link of converging and diverging lenses, and the refractive scale is the length of these lenses. Of course there are many size scales in the ISM, but the ones bigger and smaller than s_r do not have a focal point at the observer.

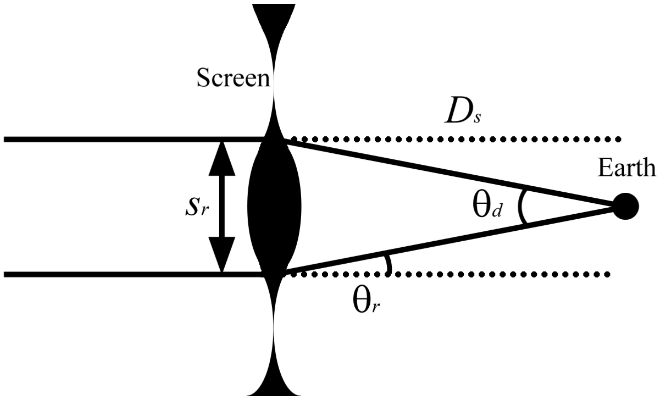

Figure 2.1 – A schematic of the thin-screen model. Rays from the pulsar reach the screen parallel to each other because the pulsar is a great distance from the screen. Each ray is refracted by no more than an angle θ_r. The diffractive angle, θ_d, subtends the refractive scale of the screen, s_r, which spans the length of a converging or diverging lens-like structure. Because the pulsar moves at a high velocity (which we assume to dominate the motion of the system), the area of the screen sampled by the pulsar changes with time.

The diffractive scale is described by the small-angle approximation of the ubiquitous diffraction formula,

$$s_d \, \theta_d \approx \lambda. \tag{2.3}$$

More precisely, the expression for s_d is[50]

$$s_d = 2 s_F \left[\frac{1}{m_B^2} \cos\left(\frac{\alpha\pi}{4}\right) \Gamma\left(1 + \frac{\alpha}{2}\right) \right]^{1/\alpha}, \tag{2.4}$$

where $s_F = \sqrt{\lambda D_s}$ is the Fresnel scale, α is the spectral slope of the screen, $\Gamma(X) = (X-1)!$ is the Gamma function, and m_B^2 is the Born Scattering Index. The DM of the screen induces

---

[a] The thermal speed in the ISM is about 10 km/s, and the length scale is about 6 AU, thus the thermal timescale is about 6 years.

a phase change of the incoming wave,

$$\Delta\phi = \frac{e^2\mathrm{DM}}{4\pi\epsilon_0 m_e c}\,\frac{1}{\nu}, \tag{2.5}$$

and the diffractive scale is the distance over which the *observed* $\Delta\phi$ changes by 1 radian (at a typical wavelength).

The diffractive and refractive scales are related by

$$s_r s_d = s_F^2. \tag{2.6}$$

As the scattering strength m_B^2 increases, the diffractive scale will shorten and the refractive scale will lengthen. Rays will be refracted by larger angles and the phase of the observed interference pattern will vary more rapidly.

Because of refraction, the point-like image of the pulsar is broadened. The scattered-broadened image, the *Scattered Brightness*, of the pulsar is the Fourier Transform (FT) of the spatial ACF of the observed electric field and is typically on the milliarcsecond scale. Without a scattering screen, the pulsar image would be micro- or nanoarcseconds in size. In an important model for this thesis, the Scattered Brightness is a Gaussian.

Observation has shown that a Gaussian Scattered Brightness alone is insufficient to reproduce a crucial observed phenomenon called a *scintillation arc*, which is a parabolic arc in the power spectrum of the pulsar's dynamic spectrum (the Secondary Spectrum)[31]. Parabolic arcs arise from interference between a Gaussian core and low-level power in a diffuse halo. A *Kolmogorov* Scattered Brightness has a core-halo character, and thus produces scintillation arcs. The fundamental difference between Gaussian and Kolmogorov Scattered Brightness functions is in the spectral slope of the scattering screen that gives rise to them. The screen for the Gaussian has a spectral slope of $\alpha = 2$ and for Kolmogorov it has a shallower slope of $\alpha = 5/3$.

Smaller inverted parabolas along the scintillation arc (called arclets) often appear in the Secondary Spectrum and can be produced by interference between discrete features in the Scattered Brightness of a pulsar. Pure Kolmogorov turbulence cannot produce this behavior, but discrete objects embedded within the Kolmogorov turbulence can cause the Scattered Brightness of the pulsar to be broken into discrete pieces. Hill *et al.*[4] suggest that these objects are compact (AU-sized), overdense structures in the ISM[b]. As the pulsar and ISM translate with respect to the Earth, the arclets translate along the scintillation arc, suggesting that the pulsar can probe these structures.

It is important to know what the axes of the Secondary Spectrum represent. If the dimensions of the dynamic spectrum are frequency ν and time t, then the Secondary Spectrum has dimensions f_ν and f_t, the Fourier conjugates of frequency and time. However, this is not very elucidating, and our analysis relies heavily on the interpretation of the conjugate

---

[b] It remains a mystery how such structures are created and sustained.

frequency as a delay. The geometric path length difference between two rays (coming from a pulsar at infinity) refracted towards the Earth (as in Fig. 2.1) is

$$\begin{aligned} \Delta L &= D_s(\cos\theta_{r,2} - \cos\theta_{r,1}) && (2.7) \\ &\approx \frac{D_s}{2}(\theta_{r,2}^2 - \theta_{r,1}^2), && (2.8) \end{aligned}$$

The difference in propagation time of these two rays is then

$$\begin{aligned} \Delta T &= \Delta L / c && (2.9) \\ &\approx \frac{D_s}{2c}(\theta_{r,2}^2 - \theta_{r,1}^2), && (2.10) \end{aligned}$$

which is the equation for the Fourier conjugate of frequency[31], f_ν. Thus the f_ν axis of the Secondary Spectrum is a differential delay. The θ^2 dependence of f_ν compared to the θ dependence of f_t causes the parabolic arcs in the Secondary Spectrum.

$$\begin{tikzcd}
{} & E(t,\nu) \arrow[l, "\mathrm{ACF}"'] \arrow[r] \arrow[d, phantom, "\upharpoonleft\!\downharpoonright"] & I(t,\nu) \arrow[r, "\mathrm{ACF}"] \arrow[d, phantom, "\upharpoonleft\!\downharpoonright"] & R_I(t,\nu) \arrow[r, mapsto] \arrow[d, phantom, "\upharpoonleft\!\downharpoonright"] & R_I(0,\nu) \arrow[d, phantom, "\upharpoonleft\!\downharpoonright"] & R_E(0,\nu) \arrow[l] \arrow[d, phantom, "\upharpoonleft\!\downharpoonright"] & R_E(t,\nu) \arrow[l, mapsto] \arrow[d, phantom, "\upharpoonleft\!\downharpoonright"] \\
{} & \widetilde{E}(f_t,f_\nu) \arrow[l] \arrow[r, "\mathrm{ACF}"] & \widetilde{I}(f_t,f_\nu) \arrow[r] & P_I(f_t,f_\nu) \arrow[r, Rightarrow] & R_h(t) & h(t) \arrow[l, "\mathrm{ACF}"'] & P_E(f_t,f_\nu) \arrow[l, Rightarrow]
\end{tikzcd}$$

Table 2.1 – Relationships to the observed Electric Field, $E(t,\nu)$. The symbol $\rightarrow$ represents a modulus square, $\Rightarrow$ represents integration over the conjugate time variable, $\mapsto$ represents the $t = 0$ slice of a function, $\leftrightharpoons$ represents a Fourier Transform, and $\xrightarrow{\mathrm{ACF}}$ represents an ACF. Implicit in these relationships is the assumption of strong scattering. Note that the mapping is cylindrical (the left wraps around to the right).

2.2 Pulsar Timing Arrays and Gravitational Waves

Linearized gravity is sufficient to predict GWs[6]. The linearization of the spacetime metric $g_{\mu\nu}$ is a small perturbation $h_{\mu\nu}$ to flat spacetime $\eta_{\mu\nu}$,

$$g_{\mu\nu} = \eta_{\mu\nu} + h_{\mu\nu}. \tag{2.11}$$

In the transverse-traceless (TT) gauge, the metric perturbation $h_{\mu\nu}$ is purely spatial, $h_{tt} = h_{ti} = 0$, traceless, $h = h_i{}^i = 0$, and transverse to the propagation vector $\mathbf{k}$, $\partial_{\mathbf{k}} h_{ij} = 0$. The linearized geodesic equation in TT gauge is

$$\frac{d^2x^i}{dt^2} = 0, \tag{2.12}$$

where t is coordinate time. Thus the *coordinate* separation between two objects, L_c, is unaffected by a GW. However, the *proper* separation, L, oscillates. For a GW propagating along the z-axis, $\hat{\mathbf{k}} = \hat{\mathbf{z}}$, with two objects separated by a coordinate distance L_c on the x-axis, their proper separation is

$$\begin{aligned} L &= \int_0^{L_c} dx \sqrt{g_{xx}} && (2.13) \\ &= \sqrt{1+h_{xx}} \int_0^{L_c} dx && (2.14) \\ &\approx \left(1+\frac{1}{2}h_{xx}\right) L_c && (2.15) \end{aligned}$$

by the binomial theorem, since $h \ll 1$ is a small perturbation. The non-zero terms of $h_{\mu\nu}$ are sinusoidal[6], so the proper separation oscillates. The fractional change in separation is then

$$\frac{\delta L}{L_c} \approx \frac{1}{2}||h_{xx}||. \tag{2.16}$$

When a GW perturbs the spacetime metric, the distance between the Earth and a pulsar at the time of emission and reception of a pulse could differ by as much as the *metric strain*, $||h_{xx}||$.

In pulsar timing, we need to know how the separation changes over time,

$$\frac{d}{dt}(\delta L) = \frac{1}{2}\left[h_{xx}(t_e) - h_{xx}(t_r)\right], \tag{2.17}$$

where t_e is the time of emission and t_r is the time of reception (at the Earth). The metric strain at any other time is inconsequential. When considering a stochastic background of GWs, the first term will be uncorrelated between pulsars because of their spatial separation, but the second term will have an angularly dependent correlation.

To determine this correlation, let $\Delta t_{m,n}$ be the m^{th} timing residual of the n^{th} pulsar, where $m = 1, \ldots, M$, and $n = 1, \ldots, N$. Each pulsar has an associated position vector $\mathbf{k}_n$ with respect to the Earth. The angle between a pair of pulsars is $\theta = \arccos(\hat{\mathbf{k}}_1 \cdot \hat{\mathbf{k}}_2)$, and the correlation coefficient between the M timing residuals of these two pulsars is

$$r(\theta) = \frac{1}{M}\sum_{m=1}^{M} \Delta t_{m,1} \Delta t_{m,2} \tag{2.18}$$

In the presence of an isotropic GW background, the ensemble-averaged correlation coefficient (the average over all pairs of pulsars as $N \to \infty$) is

$$\langle r(\theta)\rangle = \Delta t_{\text{rms}} \left[\frac{x}{4}(6\log x - 1) + \frac{1}{2}(1+\delta)\right], \tag{2.19}$$

where $x = \frac{1}{2}(1-\cos\theta)$ and $\delta = \delta(x)$ is the Dirac delta function[11] (see Fig. 2.2). Deviation from the predicted timing residual correlation is caused by sources of timing noise beyond a GW background. We are interested in the effect of timing noise in the guise of interstellar propagation delays, which are uncorrelated from pulsar to pulsar.

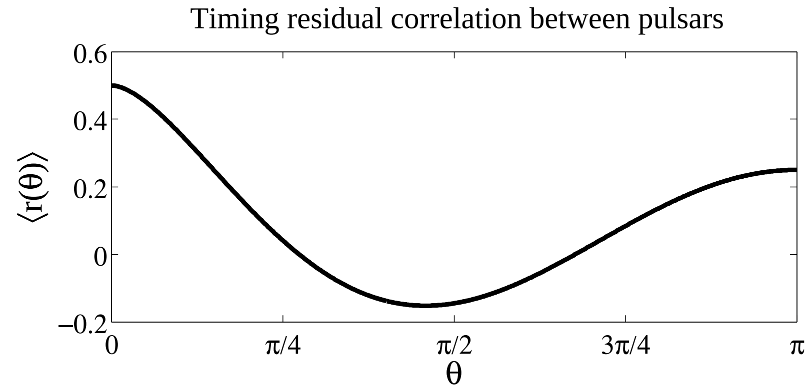

Figure 2.2 – The correlation coefficient between the sets of timing residuals for a pair of pulsars, separated by an angle θ (in radians), due to an isotropic stochastic GW background.

Chapter 3

Timing Analysis of PSR B1737+13

The pulsar PSR B1737+13 (abbreviated B1737) was observed 36 times over 38.5 weeks by Daniel Stinebring (Oberlin College) using the radio telescope at Arecibo Observatory. This pulsar was chosen for study because of the dynamic structure in its Secondary Spectrum. Indeed, the data revealed some Secondary Spectra with sharp, well-defined scintillation arcs and arclets while others were blurry and patchy; some had significant low-level power at high delay while others were concentrated near the origin, $t = 0$.

We applied a noise reduction algorithm to each Secondary Spectrum and then integrated over all fringe frequencies. The resulting quantity (power as a function of time delay) is the power spectrum of the electric field spectrum intensity and, equivalently, the autocorrelation function of the impulse response[1] (see Table 2.1). We used the centroid of this function as a measure of characteristic delay induced by the ISM. This relationship arises because the spectral domain discards all information about pulse shape. The observed pulse $p(t)$, like any signal, is an infinite series of impulses (see Fig. 3.1), and thus the spectrum we collect is of an impulse propagating through the ISM.

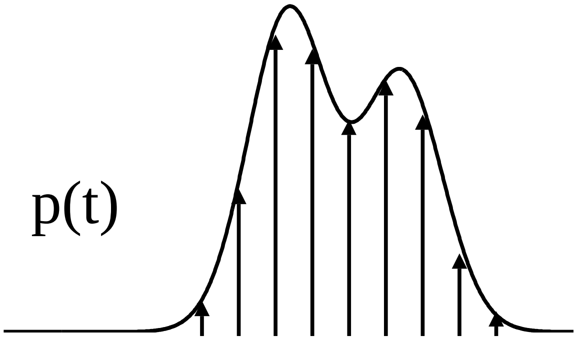

Figure 3.1 – The observed pulse, $p(t)$, is an infinite series of impulses. A caricature of this concept is shown here.

The centroid was plotted as a function of frequency and day of observation. Several major trends were discerned, whose details will be discussed in §3.2:

1) The centroids displayed an appropriate frequency scaling for scattering delays.

2) The centroid variation was consistently measurable, and the weekly variation was significantly greater than the variation during a single observation.

3) The cumulative delay identified the effect of patches of power on the centroid and tested the noise reduction algorithm (specifically, how well the background noise was removed).

Why do we call this centroid the delay induced by the ISM? The method to determine the centroid is not very elucidating, but we can transparently justify its use in a few careful steps. Motivated by the B1737 data, we invoke a $t_0\tau$ Model of the ISM in Chapter 4 to illuminate the path. In §§3.1 and 3.2, we present the observational method and results of the B1737 analysis. It will be used as a concrete reference for the following theoretical treatments.

3.1 Observational Method

We begin with a dynamic spectrum of pulsar B1737, which is the pulse intensity as a function of frequency and time, $I(t, \nu)$. Each time sample is a 10 second integration of the off-pulse spectrum subtracted from the on-pulse spectrum. At 6 samples per minute, each hour-long observation comprises about 360 spectra. The signal was monitored with a bandwidth of 50 MHz (partitioned into 2048 channels) around four different center frequencies: 1175, 1380, 1425, and 1470 MHz and processed with the Wideband Arecibo Pulsar Processor (WAPP) spectrometers.

The dynamic spectra display intricate interference patterns that vary dramatically between observations. Features called *scintles*, which are ellipsoidal intensity maxima, as well as striated crosshatchings are prominent in most. We take the square modulus of the 2D Fourier Transform (the power spectrum) of the dynamic spectrum to get the secondary spectrum.

$$P_I(f_t, f_\nu) = |\widetilde{I}(f_t, f_\nu)|^2 \tag{3.1}$$

The secondary spectra display scintillation arcs as discussed in §2.1. Some have sharp, well-defined arclets along the parabolic arc, whereas others are patchy and blurry. Some show power out to high delay; others are concentrated at zero delay. We often display a logarithmic power representation of the secondary spectrum, which accentuates the high-delay power that is completely hidden in linear plots. Only a small percentage (0.1 to 1 percent) of the power arrives after the initial spike.

Regardless of display, it remains true that there *is* power at high-delay. We are interested in a measure of the average delay of power in the secondary spectrum, and the centroid is our tool to measure it. There may not be much power at high delay, but its large lever-arm allows small amounts of power to contribute substantially to the centroid. Noise, the non-zero mean background in particular, presents a significant problem for this reason. If we are to accurately determine a centroid of the *signal*, we must remove the noise.

The robustness of spectral analysis is epitomized when a defective dynamic spectrum generates a typical secondary spectrum. The defects that ruin a dynamic spectrum do not necessarily destroy the underlying periodicities. However, one needs to be careful with discrete Fourier Transforms (DFT) because they assume a tiling of the signal. The same periodicities that made the secondary spectrum so robust can introduce FT artifact, such as overlap and sidelobes, which are minimized by windowing the dynamic spectrum[a]. We employ the "Hanning" window (Fig. 3.2).

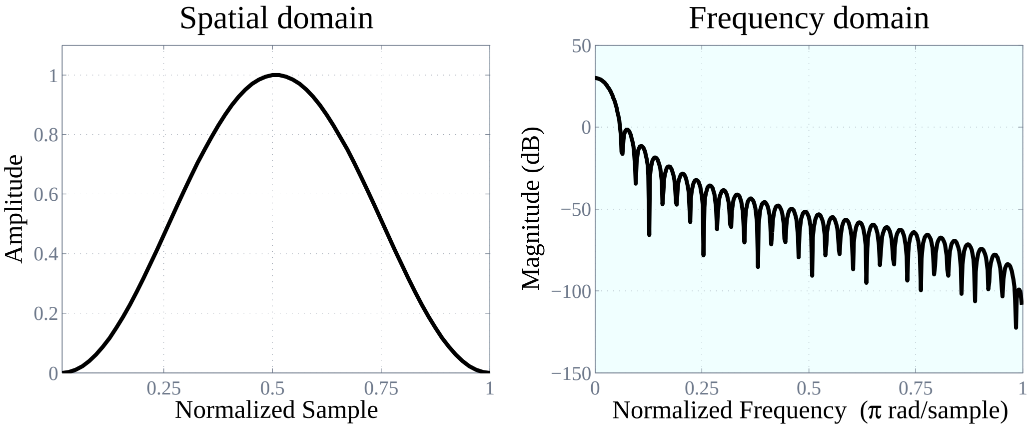

Figure 3.2 – The Hanning window (LEFT) multiplies the dynamic spectrum to reduce overlap and sidelobes in its Fourier Transform. Sidelobe attenuation is -31.5 dB, but the window introduces a broadening in the transform domain (RIGHT) due to its spectral width. The width is 4 percent of the band at -3 dB.

There are two main sources of noise in the secondary spectrum: background and FT artifacts. Because power is concentrated along the scintillation arc, there will always be regions of pixels that have an insubstantial contribution from the signal. By averaging the power in these select regions, we get an accurate measure of the background noise level, which is subtracted from every pixel in the secondary spectrum. Many methods of background noise estimation have been tried, but this one is the most universally successful. The Fourier Transform artifacts comprise a horizontal and vertical spike through the origin. The horizontal spike is removed by subtracting the average power in each row (near the origin) in a signal-free region from *every* pixel in the row. The vertical spike is the most negligible problem because it affects few to no pixels. If the noise reduction algorithm

---

[a] We must be very careful here too. *Every* manipulation to a signal, even the seemingly benign (like zero padding or resampling), has a corresponding effect in the transform domain. Everything has a trade-off. For example, windowing in one domain is equal to convolving the FT of the signal and the window in the transform domain. A window function will broaden the signal or introduce sidelobes. Choose the lesser evil for the application.

detects it, then the infected pixels are set to zero power. These regions are shown on the left in Figure 3.3.

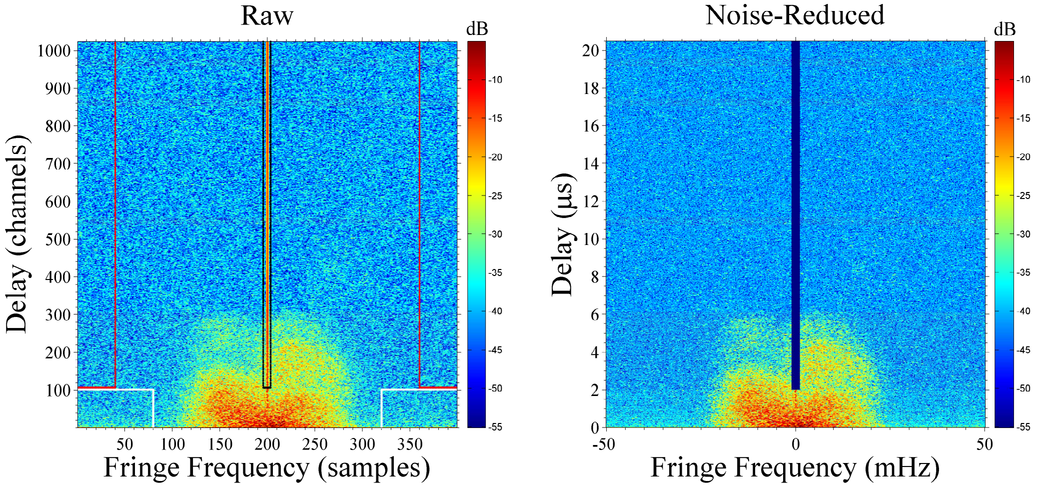

Figure 3.3 – LEFT: The Secondary Spectrum (from the 1425 MHz band on Day 122) shown before noise reduction. The red boxes indicate the regions used for background noise analysis, the white and black boxes for Fourier Transform artifact removal. RIGHT: The noise-reduced Secondary Spectrum. Because power is displayed logarithmically, but is not positive definite after processing, a lower bound was arbitrarily chosen. All values below that lower bound are colored identically to the lower bound. The effects of noise reduction are invisible on a linear power scale.

Once the mean background noise is subtracted and the artifacts are removed, the background fluctuates around zero power. This makes it difficult to display the noise-reduced secondary spectrum logarithmically because there are pixels with negative values. Nonetheless, raw and noise-reduced secondary spectra are shown in Figure 3.3.

From the noise-reduced secondary spectrum, $P_I(f_t, f_\nu)$, we integrate over all fringe frequencies (conjugate time, f_t) to get power as a function of delay only,

$$R_h(t) = \int P_I(f_t, f_\nu)\, df_t, \tag{3.2}$$

which is the ACF of the Impulse Response of the ISM (see Table 2.1). Then we calculate the integral of power with respect to delay as a function of the upper bound of delay (normalized by the total power). We call this the cumulative delay function. If T is the upper bound of delay, then cumulative delay is

$$\Gamma_{R_h}(T) = \frac{\int_0^T tR_h(t)\, dt}{\int_0^T R_h(t)\, dt}. \tag{3.3}$$

Thus, the characteristic delay induced by scattering, called Γ_R, is *the* centroid of $R_h(t)$,

$$\begin{aligned} \Gamma_R &= \lim_{T\to\infty} \Gamma_{R_h}(T) && (3.4) \\ &= \frac{\int_0^\infty t R_h(t)\,dt}{\int_0^\infty R_h(t)\,dt} && (3.5) \end{aligned}$$

The integral is expected to converge even in our finite delay interval ($T_{\mathrm{max}} = 20.4$ μs in the B1737 data), but if it doesn't, then the maximum value of the function on the interval is used as a lower bound for Γ_R.

Cumulative delay provides an important check of the noise reduction algorithm. We expect the power to diminish completely at sufficiently high delays, and therefore the cumulative delay should plateau. Barring a legitimate deviation from this assumption, we can tell if the background noise was successfully removed. If the cumulative delay never plateaus, then we have underestimated the background noise (because it continues to add more power at higher delays). If we have overestimated the background noise, the cumulative delay peaks and then begins to decline (because the background assumes a negative average). The slope of the cumulative delay where we expect no signal represents the factor by which the background noise was misestimated. Only successful background noise reduction will yield a zero-mean background and permit convergence of the cumulative delay.

We contrast the centroid analysis with another method used to calculate a time delay, which in the literature is called τ_{scatt}. Given the two-dimensional ACF of a dynamic spectrum, $R_I(t,\nu)$, the diffractive bandwidth, $\Delta\nu_d$, is the half-width at half-maximum (HWHM) of the zero time-lag slice, $R_I(0,\Delta\nu_d) = \frac{1}{2}R_I(0,0)$. Then

$$\tau_{\mathrm{scatt}} \equiv \frac{1}{2\pi\Delta\nu_d}. \tag{3.6}$$

This definition is used because the Dynamic Spectrum ACF and the secondary spectrum are Fourier Transform pairs[b], and thus obey the Localization Property[51]. To ensure that the methods are compared on an equal footing, the noise-reduced Secondary Spectrum is Fourier transformed to create the Dynamic Spectrum ACF.

$$R_I(t,\nu) = \widetilde{P}_I(t,\nu) \tag{3.7}$$

Though we used each dynamic spectrum as a whole, the analysis was repeated for temporal subsets. Specifically, the dynamic spectra were each partitioned into three spectra,

---

[b] This definition of τ_{scatt} is *exactly* Γ_R when the ACF of the Impulse Response is a double-sided exponential because the transform of a double-sided exponential (a Lorentzian function)

$$e^{-|t|/\tau} \rightleftharpoons \frac{2\tau}{1+(2\pi\nu\tau)^2}$$

is at half its initial height when $\nu = 1/(2\pi\tau)$. This is the scenario of our $t_0\tau$ Model.

with every partition spanning half an observation (and the entire spectrum). While the three dynamic spectra often displayed significantly different interference patterns, the associated secondary spectra changed imperceptibly (see Fig. 3.4). This consistency testifies to the constancy of the underlying periodicities on the timescale of a single observation. The partitioning also provides a way to monitor breakdowns in the analysis. If there is a defect in one of the spectra or if the noise reduction fails, then comparing three (semi-)independent realizations of the observation helps identify anomalous behavior. Without partitioning, there is no method to estimate the uncertainty in Γ_R.

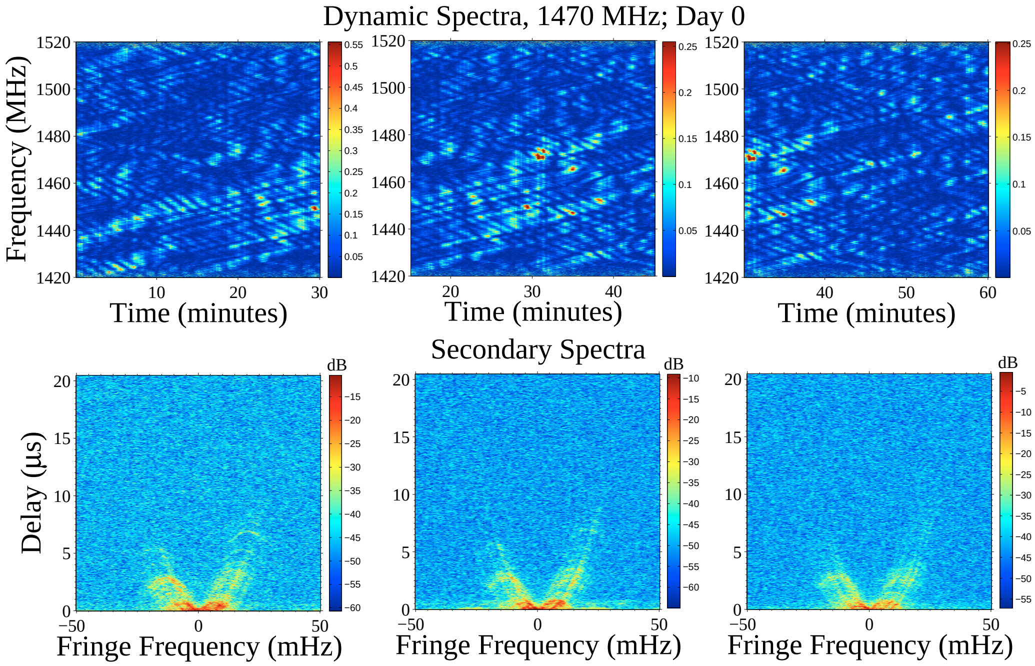

Figure 3.4 – Partitioning of the 1470 MHz observation on Day 0 into three time intervals. TOP: Three dynamic spectra. BOTTOM: Three associated secondary spectra.

3.2 Observational Results

B1737 was chosen for analysis in part because it exhibited arclets (both well-defined and patchy), which have been shown to move systematically and reliably along the parabolic arc of the secondary spectrum as the pulsar moves across the sky[4]. Since arclets constitute much (if not all) of the high-delay power, we may be able to *predict* the delay centroid of power. Unfortunately, the arclets were not seen to translate at the observation intervals because the refractive timescale (which is the relevant scale for arclet translation) was too long for a single observation and too short for the interstitial period. The observed refractive scale was between 2 and 3 days on average.

Before we make a series of observations where arclet translation *is* resolved, we need to know if arclet power will contribute enough for the centroid, Γ_R, to track the arclet motion. This question is also related to the method used to determine Γ_R. We claim that the calculation of τ_{scatt} through $\Delta\nu_d$ is a poor estimator of the characteristic delay because it is not as sensitive to power at high delay. While the centroid analysis uses the moment of each source of power, $\int tR_h(t)\,dt$, the τ_{scatt} analysis uses the total power, $\int R_h(t)\,dt$. Arclets are *high-delay, low power* features, thus $\int(\text{big})\cdot(\text{small}) \gg \int \text{small}$.

The effect of high delay arclets can be seen in a plot of Cumulative Delay. Figure 3.6 on the left displays the features that cause method-dependent delays. Figure 3.7 shows that τ_{scatt} underestimates Γ_R in a systematic fashion: when arclets are prominent at high-delay, $\tau_{\text{scatt}} < \Gamma_R$; when they are not, $\tau_{\text{scatt}} \approx \Gamma_R$. The latter, where arclets contribute insignificant power at high-delay, is shown on the right in Figure 3.6.

Apart from the systematic offset, Γ_R tracks τ_{scatt} well (Fig. 3.7), thus the Γ_R values are certainly not anomalous. The tracking of Γ_R between the center frequencies seen in Figure 3.5 attests to the robustness of the centroid timing analysis. Also, the delay exhibits the proper frequency scaling for delay due to multi-path propagation in a Kolmogorov turbulent ISM, $\tau \propto \nu^{-4.4}$, in a qualitative fashion (Fig. 3.5).

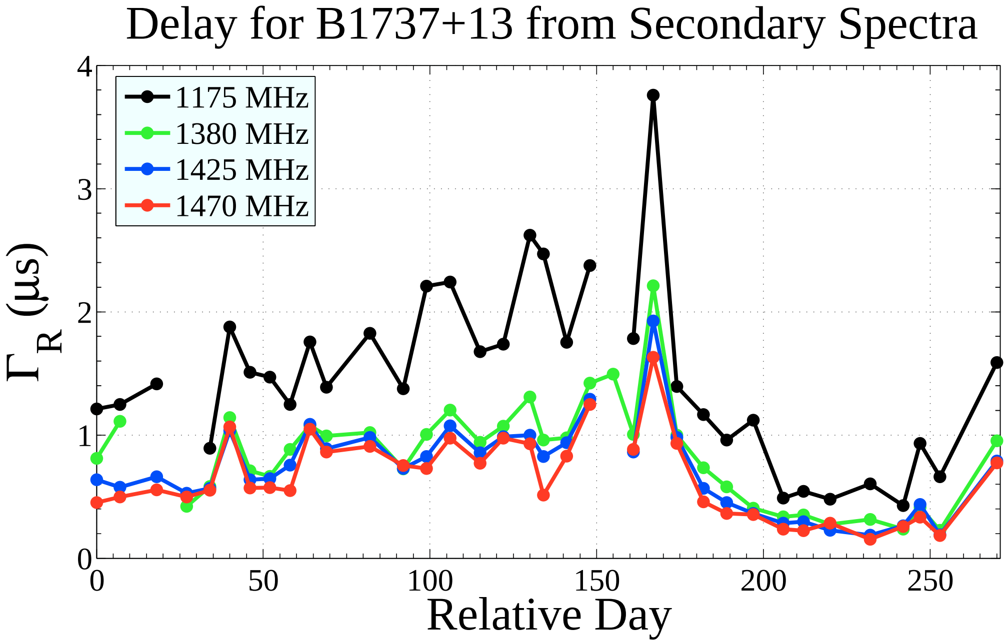

Figure 3.5 – The delays plotted are the average Γ_R of the partitions for all center frequencies for the duration of the observation.

The last point to address is the magnitude and variability of the delay, which have the most significant implications for pulsar timing. The magnitude of the delay is many hundreds of nanoseconds, which would be inconsequential if the variability was small. However, it is far from small – the delay is almost fully modulated. If the highest precision pulsar timing has an error budget of 100 ns[11], then we have already breached an era in which scattering delay cannot be ignored. And apart from some bouncing up and down, the delay varies continuously on a monthly timescale, exhibiting almost periodic behavior (with a period spanning the observation, see Figure 3.5).

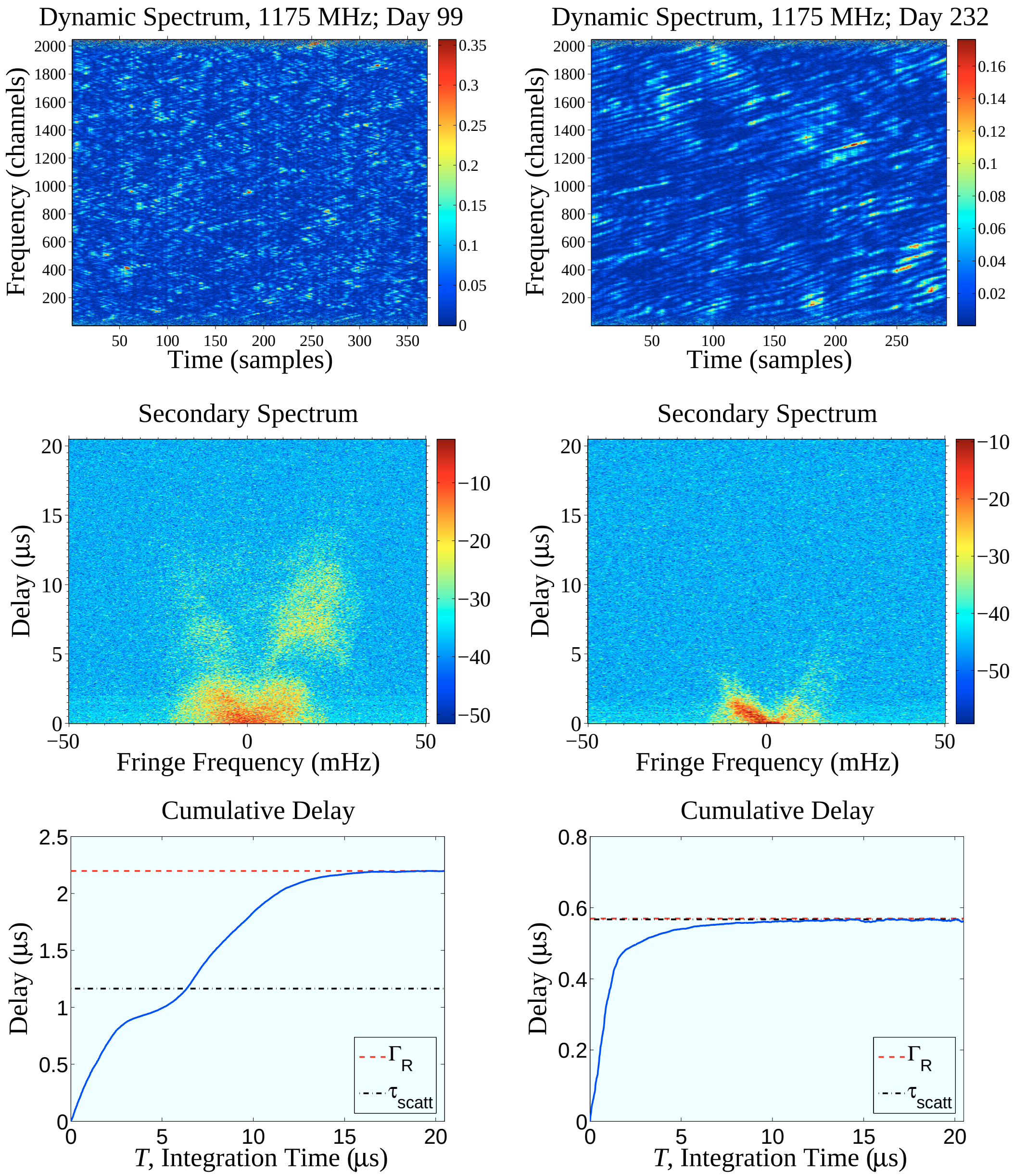

Figure 3.6 – These particular observations of B1737 (1175 MHz, Day 99 and Day 232) show how strong, high-delay arclets can affect Γ_R, the centroid of the ACF of the Impulse Response. Our analysis emphasizes the importance of such effects in pulsar timing. LEFT: Notice that the arclet between 5-11 μs increases the delay even though its power is several orders of magnitude lower than the initial spike, but that τ_{scatt} ignores it thoroughly (and thus misses almost half the delay). RIGHT: When arclets lack significant power at high-delay, τ_{scatt} is a good estimate of Γ_R.

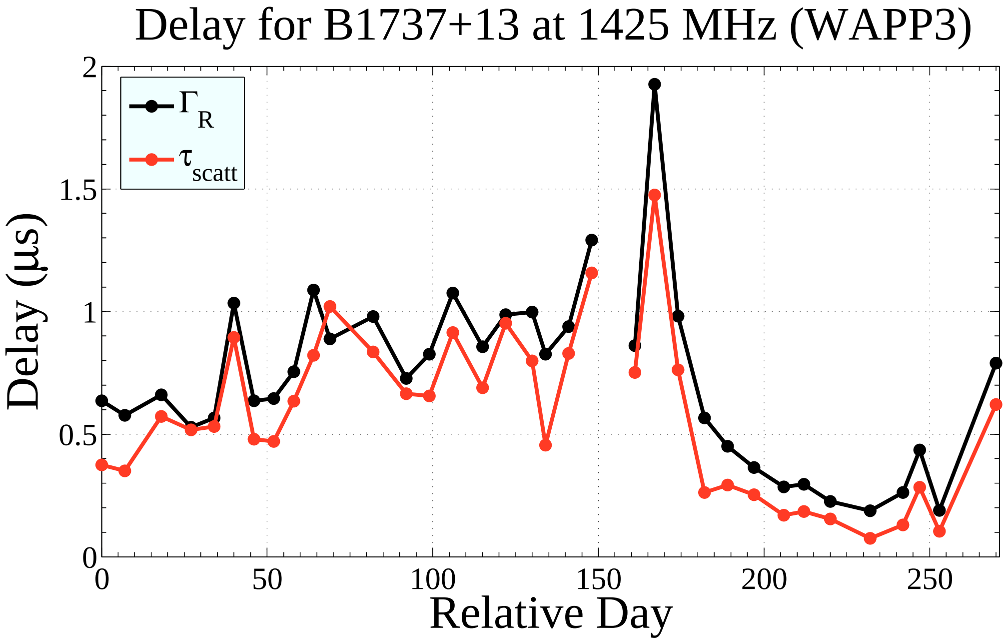

Figure 3.7 – The delays plotted are the average of the partitions. Over the entire observation, τ_{scatt} consistently underestimated Γ_R at the center frequency of 1425 MHz, and the result is qualitatively similar at 1175, 1380, and 1470 MHz. The only observation where τ_{scatt} clearly surpasses Γ_R (around Day 70) has a large uncertainty in the delay (see Fig. 3.8).

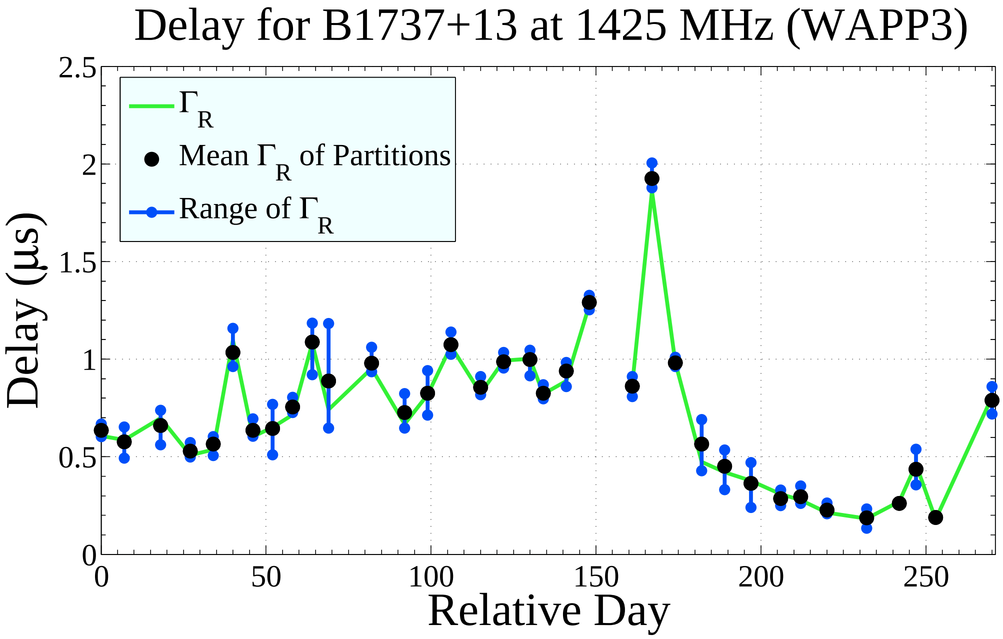

Figure 3.8 – The range of Γ_R is determined by the maximum and minimum values of Γ_R from the partitioned observation and is our estimate for the uncertainty in Γ_R.

3.3 Motivating Γ_{R_h} as a Timing Residual Correction

We have already shown that the autocorrelation function of the impulse response is the power spectrum of the intensity of the electric field spectrum, $R_h(t) = P_I(t)$. But why is the centroid of this quantity a good measure of the timing residual? Let us assume for the moment that all time delays are a result of interstellar propagation.

The popular calculation of the timing residual uses the time lag when the correlation function between an observed pulse profile and a standard profile is a maximum. The Taylor Timing Algorithm[10] (TTA) is a routine used to achieve fractional time-sample accuracy. We make the following hypotheses to motivate the equivalence of the TTA timing residual, $\Delta t(p, i)$, and the centroid of the autocorrelation function of the impulse response, Γ_R:

1) The time lag of maximum correlation between the observed pulse profile and the standard profile is the centroid of the impulse response. Thus, the timing residual is independent of the intrinsic pulse profile.

2) The autocorrelation function of a decaying exponential with a decay constant τ is also a decaying exponential with the same decay constant.

3) If the impulse response can be approximated by a decaying exponential shifted t_0 time samples from the origin, then first-order dedispersion will remove the time shift. The centroid of this corrected impulse response is now dominated by its decay constant.

The first point equates the timing residual and the centroid of the impulse response. The second and third points equate the centroid of the impulse response and the centroid of its autocorrelation function. Together, these three assertions predict that the centroid of the autocorrelation function of the impulse response is the timing residual after first-order dedispersion.

We now introduce the $t_0\tau$ Model, whose exposition will guide us along the path to prove these assertions. We use two tools to extract meaningful and realistic conclusions from the $t_0\tau$ Model approximation. The first conclusion is from a statistical treatment in §4.3 and the second is from a simulation of wave propagation through random dispersive media in Chapter 5.

Chapter 4

The $t_0\tau$ Model of the Impulse Response

The interstellar medium (ISM) is a source of error in the high-precision timing of pulsars. If we were to simplify and summarize the ISM's effect on pulsar signals, it would be this: the ISM smears the signal in time (dispersion and scattering slow the signal) and over space (the image of the pulsar on the sky appears blurred).

The smearing can only delay components of the pulsar signal because the group velocity (the speed at which a wave packet propagates) of radio waves in the ISM is less than the speed of light. This is true because the ISM is a plasma and the group velocity in a plasma is nc, where $n < 1$ (see Appendix A). From a signal processing perspective, we say that the ISM *filters* the signal. Furthermore, we know that the response of a filter to a delta function input is the impulse response, $h(t)$, and that the response of a filter to an arbitrary signal is that signal convolved with the impulse response[52].

What simplified filter should we attribute to the ISM? Geometrically, if rays are refracted an angle θ_r toward the observer by a thin screen with Gaussian phase, then the image on the sky has a Gaussian distribution[a] – fewer rays are refracted as the angle of refraction increases[53]. An image on the sky with a Gaussian distribution corresponds to an impulse response in the form of a decaying exponential (see Fig. 4.1) with a decay constant, τ, and time shift, t_0,

$$h(t) = H(t - t_0)e^{-(t-t_0)/\tau} \tag{4.1}$$

This simple expression for $h(t)$ is our $t_0\tau$ Model of the impulse response of the ISM. In reality, $h(t)$ will be a more complex function of position and a more slowly varying time T, but there is good theoretical and observational motivation for this simplification[54].

---

[a] In this context, Gaussian phase means that the electron column density is distributed in such a way that its 2D spatial ACF is functionally a Gaussian. The Gaussian image on the sky (also known as the *Scattered Brightness*) follows from the fact that its Fourier Transform is the ACF of the electric field phase, and that a Gaussian transforms into another Gaussian (see §4.1).

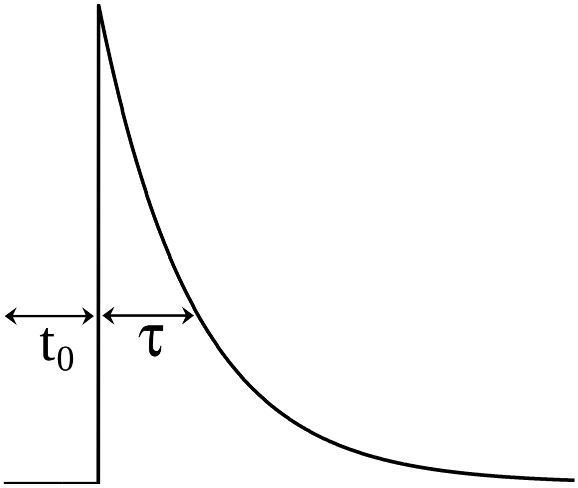

Figure 4.1 – The decaying exponential impulse response parameterized by a width τ and offset t_0. The origin, $t = 0$, is located at the left endpoint.

We can learn much about the error that the ISM induces in pulsar timing by using this $t_0\tau$ Model. Take any intrinsic pulsar signal, $i(t)$, and filter it with the $t_0\tau$ ISM. As before, the response – which is the observed pulse $p(t)$ – is the convolution of the intrinsic signal with the impulse response, $h(t)$,

$$p(t) = i(t) * h(t), \tag{4.2}$$

where $*$ denotes convolution[b]. But now we have an analytic definition of the impulse response.

The observed pulse profile is the timed quantity. By comparing it with the intrinsic profile[c], a quantitative measurement of the deviation from the unperturbed propagation can be made. We call this deviation the time of arrival *residual*. Many processes contribute to these residuals, but in our $t_0\tau$ Model, only the ISM contributes, and it does so deterministically.

Our goal, then, is to somehow *undo* the effect of the ISM filter, $h(t)$. There are two ways to determine a corrected timing residual (bearing in mind that in our $t_0\tau$ Model, the corrected residual should be zero, since we are attempting to undo the *only* effect on the pulsar signal):

---

[b] The convolution symbolism $p(t) = i(t) * h(t)$ is operationally defined as

$$p(t) = \int_{-\infty}^{\infty} i(s)h(t-s)\, ds. \tag{4.3}$$

We will see in §4.1 that convolution in one domain is multiplication in the transform domain. This is a very useful result for numerics because FTs and multiplication can be computed much faster than a direct convolution.

[c] In practice, the observed profile is compared with a *Standard* profile, $s(t)$, which is an idealization or averaged realization of the pulse profile. Here we assume that $s(t)$ approximates $i(t)$ well enough to interchange them.

1) $\Delta t(h^{-1} * p, i) = \Delta t(i, i)$

2) $\Delta t(p, i) - f(h)$

where $\Delta t(\cdot, \cdot)$ is a specific function that finds the timing residual of its first argument with respect to the second, and $f(h)$ is some function of the impulse response that characterizes the delay induced by the ISM. The motivation for these correction schemes is as follows:

1) If the impulse response can be explicitly determined, then its inverse can be used to deconvolve the observed profile,

$$h^{-1}(t) * p(t) = i(t). \tag{4.4}$$

The intrinsic pulse *by definition* contains no information about the ISM, so its timing residual is bereft of all interstellar effects. If interstellar effects dominate the timing residual (as they do in our $t_0\tau$ Model), then all errors have been corrected, and the timing residual is zero.

2) The uncorrected timing residual, $\Delta t(p, i)$, has been increased in some way by the ISM compared to $\Delta t(i, i)$, (in our $t_0\tau$ Model, this effect is described analytically by the functional form of the impulse response). The impulse response contains all the relevant information about the ISM, i.e. it describes how the timing residuals differ between the observed and intrinsic pulse profiles. If we determine how much a component of the pulse is delayed due to a convolution with $h(t)$, then we can subtract the characteristic delay from the timing residual of the observed pulse. For our $t_0\tau$ Model, the characteristic delay is simply the centroid of the impulse response, $f(h) = \Gamma_h$.

The second scheme, though more crude than the first, requires significantly less information. While the first requires knowledge of $h(t)$ in entirety to perform the deconvolution, the second scheme requires only its centroid. This is not a problem for our $t_0\tau$ Model because the impulse response is analytic, but real impulse responses are not that simple. To only need their average effect is a significant advantage. The following sections describe how we get away with using "average effect" quantities, like the impulse response's centroid, in real data analysis.

4.1 Simulating the $t_0\tau$ Model

Simplifications can be made to the timing procedure if the impulse response approximates (or in the case of the $t_0\tau$ Model, *is*) a decaying exponential with decay constant, τ, and time shift, t_0.

Simplification #1. *Though the observed pulse is the intrinsic pulse convolved with the impulse response, its timing residual is independent of the intrinsic pulse for all relevant regimes. It only changes when the impulse response changes:*

$$p = i * h, \quad \text{but} \quad \Delta t(p, i) = g(h), \tag{4.5}$$

where g(h) is some unknown function of the impulse response.

Simplification #2. *If the width of the impulse response, τ, is much smaller than the width of the intrinsic pulse, w, then the only effect of the convolution between the two will be to shift the observed pulse in time (with respect to the intrinsic pulse) by the centroid of the impulse response. Symbolically, if $\tau \ll w$, then*

$$i * h = i(t - \Gamma_h) \tag{4.6}$$

We present an analytic example to provide intuition for this result (§4.1.1), then we provide supplemental evidence with a numerical simulation (§4.1.2), and finally we consider the case when $t_0 = 0$ (§4.1.3).

4.1.1 An analytic example

The Fourier Transform of a broad function is narrow, and vice versa, so it is not surprising that the Fourier Transform of a Gaussian G with width σ is another Gaussian G' whose width is the reciprocal of the width of the original Gaussian, $\sigma' = 1/\sigma$.

Let $f(t)$ and $g(t)$ be normalized Gaussians with widths σ_f and σ_g respectively. Normalized Gaussians have the functional form $f(t)$ and Fourier Transform $F(\nu)$,

$$f(t) = \frac{1}{\sqrt{2\pi\sigma_f}} \exp\left[-\frac{1}{2}t^2\sigma_f^{-2}\right] \quad \leftrightharpoons \quad \exp\left[-\frac{1}{2}\nu^2\sigma_f^2\right] = F(\nu). \tag{4.7}$$

Then by the Convolution Theorem[52], the convolution of $f(t)$ and $g(t)$ is

$$\begin{aligned}
f(t) * g(t) &\leftrightharpoons F(\nu)G(\nu) && (4.8)\\
&= \exp\left[-\frac{1}{2}\nu^2\sigma_f^2\right] \exp\left[-\frac{1}{2}\nu^2\sigma_g^2\right] && (4.9)\\
&= \exp\left[-\frac{1}{2}\nu^2(\sigma_f^2 + \sigma_g^2)\right] && (4.10)\\
&= \exp\left[-\frac{1}{2}\nu^2\sigma_c^2\right] && (4.11)\\
F(\nu)G(\nu) &\leftrightharpoons \frac{1}{\sqrt{2\pi\sigma_c}} \exp\left[-\frac{1}{2}t^2\sigma_c^{-2}\right] && (4.12)
\end{aligned}$$

That is, the convolution is another Gaussian with width

$$\begin{aligned}
\sigma_c^2 &= \sigma_f^2 + \sigma_g^2 && (4.13)\\
\sigma_c &= \sigma_f\sqrt{1 + \left(\frac{\sigma_g}{\sigma_f}\right)^2}. && (4.14)
\end{aligned}$$

Let us now assume that one of the widths is significantly smaller than the other, $\sigma_g \ll \sigma_f$. Then using the binomial expansion,

$$\sigma_c \approx \sigma_f \left[1 + \frac{1}{2}\left(\frac{\sigma_g}{\sigma_f}\right)^2\right]. \tag{4.15}$$

For specificity, assume $\sigma_f = 1$ and $\sigma_g = 1/1000$. Thus, the width of the convolution is

$$\sigma_c \approx \left[1 + \frac{1}{2}\left(\frac{1}{1000}\right)^2\right] = 1 + \left(5 \times 10^{-7}\right). \tag{4.16}$$

Even though $g(t)$ was one-thousandth the width of $f(t)$, the width of the convolution is only greater than that of $f(t)$ by less than one-millionth.

For this example it is sensible to regard $f(t)$ as a signal and $g(t)$ as a filter. While both functions can play either role, the wider function, f, is being acted upon – it is broadened by the filter. In our application to pulsar timing, an intrinsic pulse can be orders of magnitude wider than the impulse response, its filter. The narrowest observed pulse is about 40 μs at FWHM[55], whereas we are trying to show that impulse responses may have widths on the order of 1 μs at GHz frequencies (see §3.2). Thus we will remain in regimes where

$$\frac{\tau}{w} \lesssim \frac{1}{10} \tag{4.17}$$

To summarize, the broadening due to convolution is proportional to the square of the ratio of widths of the convolution inputs,

$$(\sigma_c - \sigma_f) \ \propto \ (\sigma_g/\sigma_f)^2. \tag{4.18}$$

This is no trickery of Gaussian functions in particular. *Any* two functions whose widths are disparate enough will convolve similarly.

4.1.2 A numerical simulation

A noiseless intrinsic pulse profile and impulse response were generated. While I will reference a Gaussian intrinsic pulse and a decaying exponential impulse response, the simulation was run with the following variants to the same effect:

Intrinsic Pulse

1) Gaussian, e^{-t^2/w^2}

2) Superposition of multiple Gaussians, $\sum_n A_n e^{-t^2/w_n^2}$

Impulse Response

1) Decaying exponential, $H(t-t_0)e^{-(t-t_0)/\tau}$

2) One-sided Gaussian, $H(t-t_0)e^{-(t-t_0)^2/\tau^2}$

3) Kolmogorov response, $H(t-t_0)\int_0^\infty se^{-s^{5/3}}J_0(s\sqrt{t-t_0})\,ds$

where $J_0(\cdot)$ is the Bessel function[d]. The intrinsic pulse width was fixed at $w = 50$ time samples and the width ratio τ/w was incremented in a series of simulations from a ratio of 10^0 to 10^{-3}.

The intrinsic pulse was convolved with the impulse response, creating the observed pulse (see Fig. 4.2). The TTA was then used on the observed pulse to determine the time of arrival, $\Delta t(p,i)$, compared to that of the intrinsic pulse, $\Delta t(i,i)$.

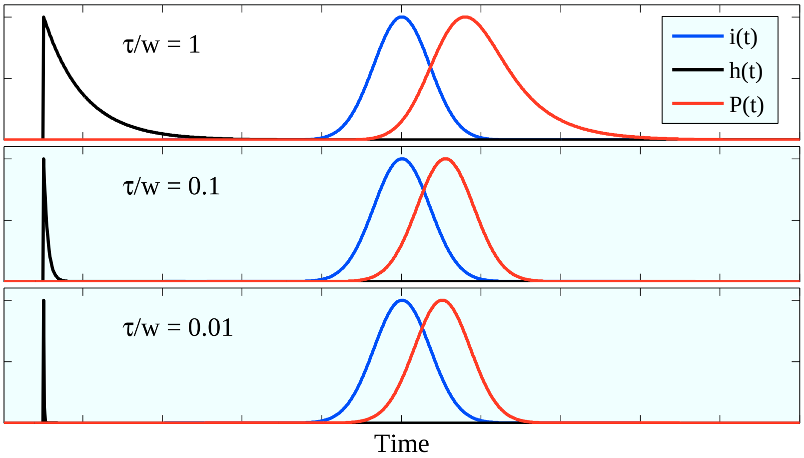

Figure 4.2 – The intrinsic pulse (blue), $t_0\tau$ impulse response (black), and observed pulse (red) are shown for three different widths of the impulse response. On the top, the width is large relative to the width of the intrinsic pulse, so the observed pulse has a broadened tail. On the bottom, the width is small relative to the width of the intrinsic pulse, so the observed pulse is approximately a shifted copy of the intrinsic pulse. Note that $h(t)$ has a non-zero value of t_0 (5% of the interval) because $t = 0$ at the left endpoint.

The TTA uses spectral analysis[e] of its arguments (here the observed and intrinsic pulses) to determine the change in time of arrival to within a fraction of a time sample. It is the predominant timing algorithm in pulsar timing routines.

We extract two major conclusions from this noiseless simulation where the intrinsic pulse profile is stable and the only source of timing error is interstellar propagation:

1) *The timing residual is given by the centroid of the impulse response, Γ_h.* The particular shape of the intrinsic pulse is inconsequential because $\Delta t(p,i) = \Gamma_h$ when $\tau/w \lesssim 1/10$, which is the upper bound of the observational regime. The simulation results

---

[d] The third impulse response is thought to be a better approximation for the ISM than our $t_0\tau$ Model[2] (the first impulse response).

[e] Note that this analysis, though performed in the transform domain, is not related to our timing analysis.

comparing $\Delta t(p,i)$ and Γ_h for a range of width ratios are shown in Figure 4.3. This justifies **Simplification #1**.

2) *When the intrinsic pulse is much wider than the impulse response, the observed pulse is essentially the intrinsic pulse shifted by the centroid of the impulse response.* The timing residual is constituted by a shift and a broadening regardless of the width ratio. The fact that the observed pulse for $\tau/w = 1$ in Figure 4.2 is visibly smeared implies that it must be shifted less than Γ_h. At the other extreme, the fact that the observed pulse for $\tau/w = 0.01$ is imperceptibly smeared implies that it must be shifted almost *entirely* by Γ_h. Quantitatively, both statements are true. This justifies **Simplification #2**.

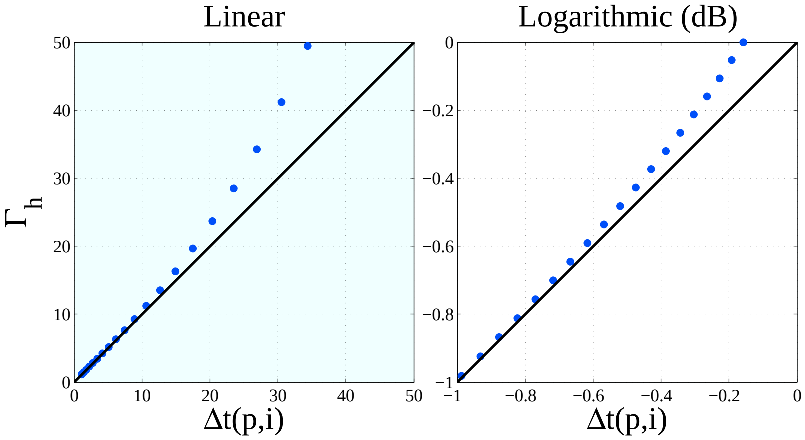

Figure 4.3 – A set of timing residuals and centroids are plotted for various width ratios (from 10^{-3} to 10^{0}), where the intrinsic pulse width is $w = 50$ time samples. We can set t_0 to zero for convenience without loss of generality, and then $\tau = \Gamma_h$. The data is not shown below a width ratio of 10^{-1} because there it simply coincides with the diagonal.

These conclusions can be summarized in a set of short symbolic equations.

$$\begin{aligned}\Delta t(p,i) &= \Delta t(i*h,i) && (4.19)\\ &= \Delta t(i,i)+\Gamma_h && (4.20)\\ &= \Delta t(i,i)+(\text{shift}+\text{broadening}) && (4.21)\end{aligned}$$

Notice that we have also validated the “crude” scheme (given as No. 1 on page 27) to undo the effect of the ISM, since

$$\Delta t(p,i)-\Gamma_h = [\Delta t(i,i)+\Gamma_h]-\Gamma_h = \Delta t(i,i). \tag{4.22}$$

When the width of the impulse response, τ, is much less than the width of the intrinsic pulse, w, we have

$$\begin{aligned}\text{shift} &\approx t_0+\tau && (4.23)\\ \text{broadening} &\approx \left(\frac{\tau}{w}\right)^2 w && (4.24)\end{aligned}$$

where the latter comes from Eq. 4.15. Thus for $\tau \ll w$, the broadening will be negligible and the shift will be the centroid. Notice that we are forcing τ to be small, so the centroid (and thus the shift in the observed pulse) could be dominated by the offset t_0 (the shift in the impulse response). This would happen identically if the impulse response were a delta function.

4.1.3 The $t_0 = 0$ case

Motivated by observations, consider the case in which t_0 is zero (i.e. *there is no offset in the impulse response*). The centroid of the impulse response is dominated by its width, τ, but let τ still be small compared to the width of the pulse[f].

A Discussion. We simulated more realistic conditions by limiting the time resolution and including a finite signal-to-noise ratio (SNR). We used Gaussian noise with standard deviation σ_{noise} and defined our SNR as

$$\text{SNR} \equiv \frac{p_{\max}}{\sigma_{\text{noise}}}, \tag{4.25}$$

where $p_{\max}$ is the maximum power of the observed pulse.

By fully sampling the (τ, SNR) state space (see Fig. 4.4), we determined that the fractional uncertainty in the pulse power determines the fractional uncertainty in the pulse timing,

$$\frac{\sigma_{\text{noise}}}{p_{\max}} \approx \frac{\delta(\Delta t)}{w}. \tag{4.26}$$

Substituting in SNR and solving for $\delta(\Delta t)$, the uncertainty in the timing residual is

$$\delta(\Delta t) \approx \frac{w}{\text{SNR}} \tag{4.27}$$

Thus a correction is only useful when the induced delay is larger than the uncertainty in the timing residual, $\tau > \delta(\Delta t)$, otherwise the correction is buried in the noise. To ensure that $\tau > \delta(Dt)$, the width ratio τ/w or the SNR must be large. This implies that the spectral timing analysis is crucial – it provides delay information, Γ_R, that is difficult to determine in the time domain in the presence of noise. There is a caveat, though. Regardless of our sensitivity to an interstellar delay, a correction is trivialized when it is smaller than the noise.

A Comment. The pulsar timing community has a tendency to ignore non-dispersive interstellar propagation effects until the observed pulse is *visibly* broadened by $h(t)$, as in the top panel of Figure 4.2. However, we have shown (analytically and by simulation) that the effect of $h(t)$ when its width is much smaller than the pulse width, $\tau \ll w$, is to shift

---

[f] The observationally relevant constraint $\tau \gg t_0$ is justified in section §5.2, where dedispersion is discussed. Furthermore, t_0 need only be constant for this discussion to be relevant because only *variation* in timing behavior matters. If t_0 is constant, we simply redefine where $t = 0$ so that the constant is zero.

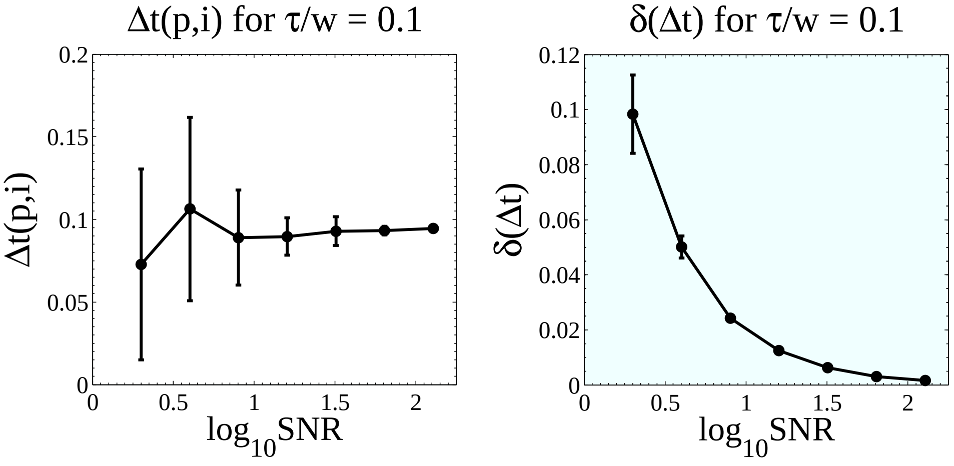

Figure 4.4 – A representative width ratio of $\tau/w = 0.1$ is shown. LEFT: As the SNR increases, the uncertainty in $\Delta t(p,i)$ decreases, and the mean value settles down to the value shown in Figure 4.3, where SNR (defined in Eq. 4.25) is infinite. RIGHT: The uncertainty behaves as described in Eq. 4.27.

the intrinsic pulse by the centroid of $h(t)$,

$$i(t) * h(t) = i(t - \Gamma_h). \tag{4.28}$$

There is no smearing, no "scattering tail" to see[g]. Thus, there is no method in the time domain to determine what $h(t)$ has actually done because there is only a shift. Yes, the shift *will* register in the timing residual from the TTA, but there's no telling what the *source* of the shift was, whether it was interstellar scattering or gravitational wave perturbations.

Though a shift in the intrinsic pulse by Γ_h is imperceptible in the time domain, it has a non-negligible effect on the timing residuals that can be precisely determined in the spectral domain. Furthermore, the spectral domain analysis provides *independent information* of the scattering delay. For instance:

1) Let us assume that the only timing error resulted from scattering. Then the TTA would find a timing residual $\Delta t = x$ and we would find a scattering delay $\Delta t_s = x$ with the spectral domain technique. Thus we can claim that the only timing effect is scattering.

2) Now let us assume that both scattering and gravitational waves are sources of timing error. The TTA will find a timing residual $\Delta t = x$, but we would find a scattering delay $\Delta t_s = y$. We can thus confirm the existence of gravitational waves and declare that they have an amplitude such that they induce a timing error $\Delta t_{\text{GW}} = \Delta t - \Delta t_s$.

---

[g] When there *is* a scattering tail to see, the broadening is measured in the time domain by fitting decaying exponentials to the scattering tail. This complicated procedure must account for the pulsar-specific intrinsic pulse embedded within the observed pulse. The spectral analysis that we employ is a much more direct (and unambiguous) measurement.

While our technique does not allow us to (directly) determine a t_0 component of the centroid of the impulse response (which is why we stipulated that t_0 was negligible for the discussion and comment), such a component is the first order term from dispersion. If we can successfully dedisperse the signal, then the centroid *will* be dominated by τ, and the spectral timing analysis *will* determine the centroid of the dedispersed impulse response.

There is another important step to take before we can claim that the centroid of the impulse response is the quantity that we are probing with our spectral domain analysis. We take that step now.

4.2 The Autocorrelation Function of the Impulse Response

We have so far motivated the centroid of the impulse response $\Gamma_h(t)$ as a correction factor for interstellar effects in pulsar timing, but this quantity is not an observable[h]. To bridge the final gap between the ideal and the real, we invoke the autocorrelation function (ACF) of the impulse response, $R_h(t)$, which *is* an observable. In this section, we motivate the use of its centroid, Γ_{R_h}, as the interstellar scatter correction factor.

The $t_0\tau$ Model approximated the impulse response as a decaying exponential characterized by a width τ and offset t_0. Its centroid is their sum,

$$\Gamma_h = t_0 + \tau. \tag{4.29}$$

The ACF of the impulse response is characterized *only* by its width, τ (which is the same width as the impulse response) because any time shift information is lost in the process of autocorrelation:

$$\begin{aligned} R_h(t) &= \int_{t_0}^{\infty} h(s)h(s+t)\,ds && (4.30)\\ &= \int_{t_0}^{\infty} e^{-(s-t_0)/\tau}e^{-(s+t-t_0)/\tau}\,ds && (4.31)\\ &= e^{-t/\tau}\left(\frac{\tau}{2}\right) && (4.32)\end{aligned}$$

Thus, we see that the centroid of $R_h(t)$ approximates the centroid of $h(t)$ when $\tau \gg t_0$.

Sadly, there is no observational evidence that $\tau \gg t_0$. Furthermore, as a real impulse response diverges from the $t_0\tau$ Model, so too does the equivalence between the width of $h(t)$ and its ACF. However, removing a time offset from each impulse response can be accomplished with first-order dedispersion (which removes a linear phase ramp, i.e., by the Fourier Shift Theorem[52], a constant time offset). After first-order dedispersion, the $t_0\tau$ impulse response is *identical* to its ACF.

---

[h] This is a result of instruments measuring signal intensity without phase information, which is buried in noise.

4.3 A Statistical Correction

In pulsar timing, the variance of a set of timing residuals determines its quality. With all timing effects accounted for, the variance of residuals would be zero. Given the following:

1) The $t_0\tau$ Model, $\Gamma_h = t_0 + \tau$,

2) A set of timing residuals, Δt_j, and

3) A set of $h(t)$ widths, τ_j, calculated from the centroid of $R_h(t)$,

we can make a correction to the timing residuals with the observationally accessible delay, τ. One might assume that a good corrected timing residual would be

$$\Delta t'_j = \Delta t_j - \tau_j. \tag{4.33}$$

Unfortunately, this is not always helpful. For instance, if $t_0 = -\tau$, then

$$\begin{aligned} \Delta t'_j &= \Delta t_j - \tau_j & (4.34) \\ &= (t_{0,j} + \tau_j) - \tau_j & (4.35) \\ &= -\tau_j & (4.36) \end{aligned}$$

whereas the *uncorrected* timing residual is $\Delta t_j = 0$ because $\Delta t = \Gamma_h$ in the $t_0\tau$ Model! How unfortunate.

To intelligently correct, we must know statistically how t_0 compares to τ. In particular, if we know τ exactly, then the quality of a statistical correction to Γ_h depends on how precisely we know the relative variation of t_0, $R = \sigma_{t_0}/\sigma_\tau$, and the correlation coefficient between t_0 and τ, $\rho(t_0, \tau)$.

Though τ is an observable, t_0 is not. How then can we get *any* estimate of the variance of t_0 and its correlation coefficient with τ? The answer lies in simulation. With access to the impulse response (and thus the set of $t_{0,j}$ and τ_j), we can determine if there is any consistent variance or correlation that can be applied when we do not have access to the set of $t_{0,j}$. The following analysis will show how well we can improve the timing residuals, and how precisely we need to know the statistical quantities to do so.

Conscious of our misguided attempt in Eq. 4.33, we can best correct the timing residuals not by strictly subtracting τ, but by subtracting a multiple, $\alpha\tau$. The coefficient α must be derived from the available statistical information. Let F be the ratio of the corrected to uncorrected timing residuals,

$$F = \frac{Var(\Gamma_h - \alpha\tau)}{Var(\Gamma_h)}, \tag{4.37}$$

where $\alpha \in \mathbb{R}$. Minimizing F minimizes the timing residuals (since $\Gamma_h = \Delta t$). The residuals have improved if $F < 1$, and we have perfectly corrected if $F = 0$ (because F is positive definite, a ratio of squared quantities).

If we continue to write F out more explicitly and invoke the $t_0\tau$ Model, then

$$F = \frac{Var\left[(t_0+\tau)-\alpha\tau\right]}{Var[t_0+\tau]} \tag{4.38}$$

$$= \frac{Var(t_0)+(1-\alpha)^2 Var(\tau)+2(1-\alpha)Cov(t_0,\tau)}{Var(t_0)+Var(\tau)+2Cov(t_0,\tau)} \tag{4.39}$$

Adopting the sigma notation for variance and covariance, e.g. $Var(X)=\sigma_X^2$,

$$F = \frac{\sigma_{t_0}^2+(1-\alpha)^2\sigma_\tau^2+2(1-\alpha)\sigma_{t_0,\tau}}{\sigma_{t_0}^2+\sigma_\tau^2+2\sigma_{t_0,\tau}} \tag{4.40}$$

$$= 1+\frac{\alpha^2\sigma_\tau^2-2\alpha(\sigma_\tau^2+\sigma_{t_0,\tau})}{\sigma_{t_0}^2+\sigma_\tau^2+2\sigma_{t_0,\tau}} \tag{4.41}$$

$$\tag{4.42}$$

We introduce again the relative standard deviation of t_0, R, and the correlation coefficient, ρ, between t_0 and τ.

$$R = \frac{\sigma_{t_0}}{\sigma_\tau} \tag{4.43}$$

$$\rho = \frac{\sigma_{t_0,\tau}}{\sigma_{t_0}\sigma_\tau} \tag{4.44}$$

Note that $-1 \le \rho \le 1$. Then F can finally be reduced to

$$F = 1+\frac{\alpha^2-2\alpha(1+R\rho)}{1+R^2+2R\rho} \tag{4.45}$$

Our naïve attempt to subtract τ from Δt (in Eq. 4.33) is the special case when $\alpha=1$. What statistical regimes would benefit from such a blind correction? Well, when $\alpha=1$,

$$F_{\alpha=1}=\frac{R^2}{1+R^2+2R\rho}. \tag{4.46}$$

We make an improvement if $F<1$.

$$1 > \frac{R^2}{1+R^2+2R\rho} \tag{4.47}$$

$$\rho > -\frac{1}{2R} \tag{4.48}$$

We postulated the $t_0=-\tau$ scenario, in which $R=1$ and $\rho=-1$. Thus, $-1>-\frac{1}{2}$ is false, and we confirm that we *decrease* the timing residual quality with our correction: $Var(\Delta t') > Var(\Delta t)$.

In general, i.e. for any $\alpha\in\mathbb{R}$, we can define the region in which an improvement is made, and we can identify the value of α that minimizes the timing residuals for a particular set of statistics. So, for any α, we have made an improvement if $F<1$.

$$1 > 1+\frac{\alpha^2-2\alpha(1+R\rho)}{1+R^2+2R\rho} \tag{4.49}$$

$$\rho > \frac{\alpha-2}{2R} \tag{4.50}$$

so long as $\alpha \neq 0$ and $1 + R^2 + 2R\rho \neq 0$. We have made the *best* improvement when F is a minimum.

$$\begin{aligned} \frac{\partial F}{\partial \alpha} &= 0 && (4.51) \\ 0 &= \frac{2\alpha - 2}{1 + R^2 + 2R\rho} && (4.52) \\ \alpha &= 1 + R\rho && (4.53) \end{aligned}$$

Using this critical value of α (Eq. 4.53), we can achieve a minimum value for F of

$$F_{\text{min}} = \frac{(1-\rho^2)R^2}{1 + R^2 + 2R\rho}. \qquad (4.54)$$

In addition to suggesting a set of $\alpha\tau_j$ to subtract from $\Gamma_{h,j}$, this result provides immediate intuition into how well we can do if we only rely on the statistics of t_0. Because of the $(1-\rho^2)$ term, the correction is perfect, $F = 0$, when $|\rho| = 1$ for any R[i]. When $R \gg 1$, the improvement is best as $|\rho|$ increases. But there is *always* improvement, except on the infinitesimal subspace of the (R, ρ) parameter space when $\rho = -1/R$. On this curve, there is no improvement ($F = 1$). The details can be seen in Figure 4.5.

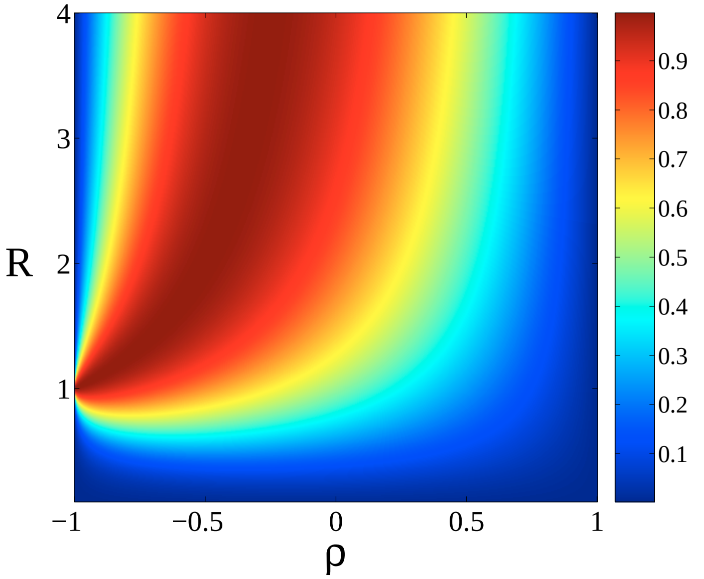

Figure 4.5 – F_{min}, the *best* improvement that can be made to timing residuals if the statistics of t_0 (ρ and R) are known precisely. The lower the value of F, the better the improvement.

It now rests upon the simulation to determine if there are any statistical relationships between t_0 and τ so that this result can be used. However, the simulation may not reveal

---

[i] However, $F = 1 \neq 0$ when $\rho = -1$ and $R = 1$ by l'Hôpital's Rule. This is a degenerate case of the solution. Fortunately the coefficient of τ subtraction for this case, $\alpha = 1 + R\rho = 0$ still perfectly corrects the timing residuals. This was the result of the initial example starting with Eq. 4.34.

an exact relationship. We would prefer something definite, like $R = 7.3$ and $\rho = 0.88$, which dictates an $\alpha = 7.424$. More likely is $R = 7 \pm 1$ and $\rho = 0.9 \pm 0.1$, which suggests an $\alpha = 7 \pm 2$. How sensitive is the improvement to the uncertainty in α?

In general, this is a difficult question to answer and visualize. Let us assume that one of the statistical parameters is well known, say ρ. Then we extract a constant ρ slice of F. There exists a true $R = R_0$ and a corresponding best $\alpha_0 = 1 + R_0\rho$. The sensitivity of F to α is the amount that α can vary about α_0 while $F < 1$ is still true. In some of the parameter space, there is much flexibility in the value of α. In others, it is critical to determine α precisely. Two examples are provided in Figure 4.6, and the pair on the right mimics the above example where $R \approx 7$ and $\rho \approx 0.9$.

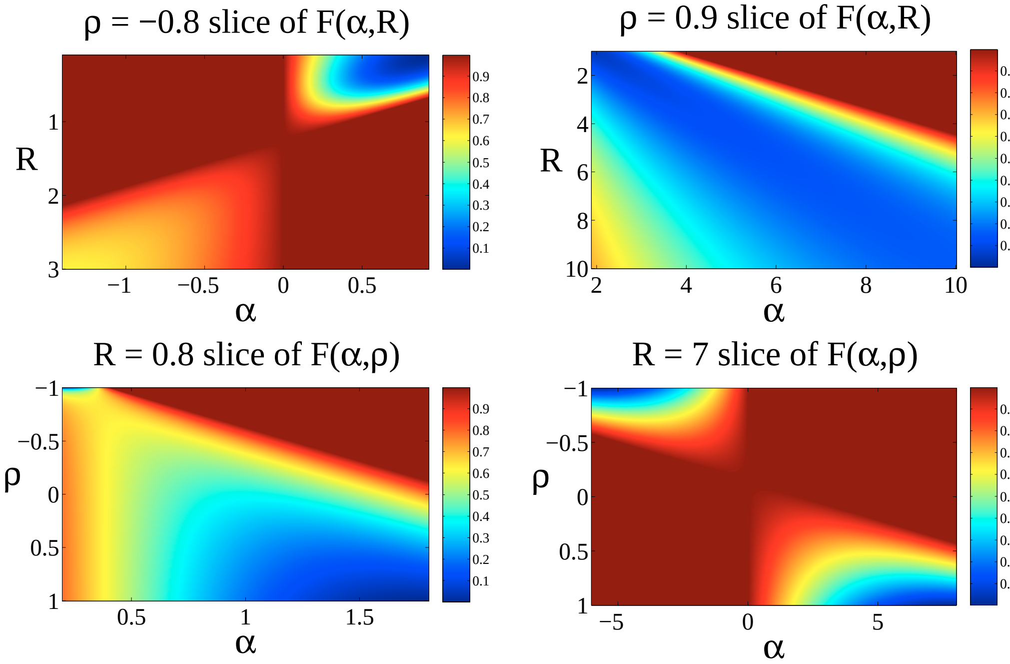

Figure 4.6 – Sensitivity of F to uncertainty in statistical parameters. Regions in red show parameter combinations that result in degraded timing residuals after correction using the associated α. In the top right figure, let's assume that the true $R_0 = 7$. Then α can be between 5 and 9 and *still* result in an $F < 0.4$.

Chapter 5

Dispersion and the Simulation

The Coles Simulation[50] is a wave-propagation simulation that we use to investigate quantities that are not observable with a telescope. In particular, we want to know how the true time delay Γ_h correlates with observables, such as Γ_R. The advantage of the Coles Simulation over ray-tracing simulations[49] is that it permits both refractive and diffractive effects.

During a single call to the program, N_ν plane wave simulations are run independently. Each plane wave is incident upon a two-dimensional screen and exits with corrugations in phase dictated by the screen. After propagating to an observer plane, this corrugated wave is one of the N_ν outputs of the simulation, which are concatenated to simulate the propagation of a wave packet.

If the screen is uniform, then the phase of the exiting plane wave is not corrugated. There is no spatial variation in the phase advancement, only the frequency variation due to dispersion – a higher frequency plane wave is advanced in phase less than a lower frequency plane wave[a].

All phase changes are related to a physical quantity, the column density electrons, also known as Dispersion Measure (DM),

$$\mathrm{DM} = \int n_e \, d\ell. \tag{5.1}$$

As derived in Appendix A, a plane wave is advanced in phase (in mks units) by

$$\Delta\phi = \frac{e^2 \Delta\mathrm{DM}}{4\pi\epsilon_0 m_e c} \, \frac{1}{\nu}. \tag{5.2}$$

If the waves are given by their wavelength,

$$\Delta\phi = \frac{e^2 \Delta\mathrm{DM}}{4\pi\epsilon_0 m_e c^2} \, \lambda. \tag{5.3}$$

---

[a] In any scenario, the wave is only dispersed immediately upon exiting the screen. Higher-order effects due to *non-uniform* spatial structure in the screen, such as scattering, arise from the propagation of the wave to the observer plane.

Thus, dispersion causes phase to advance linearly with wavelength (a phase ramp).

To correct for dispersion – to *dedisperse* – the phase ramp must be subtracted from the electric field phase[b]

$$E' = E e^{-i\Delta\phi(\lambda)}. \tag{5.4}$$

If the bandwidth is narrow enough, then

$$\nu^{-1} \approx c_1\nu + c_2, \tag{5.5}$$

and the phase advancement is linear in frequency as well. In this case, the dedispersed electric field is

$$E' \approx E \cdot \exp\left[2\pi i(c_1\nu + c_2)\right] \tag{5.6}$$

How does this relate to pulsar timing and the time domain? The Fourier Shift Theorem states that a linear phase ramp in frequency is a constant time shift.

$$\exp\left[2\pi i(c_1\nu + c_2)\right] \;\leftrightharpoons\; h(t + c_1). \tag{5.7}$$

Thus we have discovered that the first-order effect of dispersion is to induce a time shift c_1 in the Impulse Response. We can immediately conclude that the ACF of the Impulse Response completely ignores first-order dispersion. The ACF centroid, Γ_R, is affected only by scattering and higher-order dispersive effects.

Revisiting the $t_0\tau$ Model, this time shift c_1 is t_0. After first-order dedispersion, the centroid of the impulse response changes from Eq. 5.8 to Eq. 5.9:

$$\begin{aligned} h(t) &= H(t-t_0)e^{-(t-t_0)/\tau} && (5.8)\\ h(t+t_0) &= H(t)e^{-t/\tau} && (5.9) \end{aligned}$$

And the centroid of the dedispersed Impulse Response *is* the centroid of its ACF,

$$\Gamma' = \Gamma - t_0 = \tau \tag{5.10}$$

5.1 Ideal Dedispersion

A series of plane waves that are evenly spaced in wavelength can be dedispersed immediately upon exiting the screen by first determining how much phase advancement occurred for a particular wavelength and then scaling it linearly for all other wavelengths. This would provide a phase $\Delta\phi_j$ to subtract from the j^{th} wave. This simplicity arises because dispersion is deterministic.

---

[b] In this chapter we define a primed symbol as the dedispersed counterpart of the unprimed symbol (i.e. E = dispersed vs. E' = dedispersed).

Consider an attempt to align the phase of all the spectral channels with the center channel, call it λ_c. Since $\Delta\phi \propto \lambda$, we can write

$$\frac{\Delta\phi_j}{\lambda_j} = \frac{\Delta\phi_c}{\lambda_c}, \tag{5.11}$$

where λ_j and $\Delta\phi_j$ are the wavelength and phase of the j^{th} spectral channel, where j goes from 1 to N_ν. Then

$$\begin{aligned}\Delta\phi_j - \Delta\phi_c &= \left(\frac{\lambda_j}{\lambda_c} - 1\right)\Delta\phi_c & (5.12)\\ &= \left(\frac{[\lambda_1 + (j-1)\Delta\lambda]}{\lambda_c} - 1\right)\Delta\phi_c & (5.13)\end{aligned}$$

where $\Delta\lambda$ is the constant separation in wavelength between consecutive spectral channels[c] such that $N_\nu\Delta\lambda$ is the total bandwidth of the simulation and λ_1 is the wavelength at the beginning of our band, i.e. $\lambda_1 = \lambda_c - \frac{1}{2}N_\nu\Delta\lambda$. Finally, we define d_λ as the fractional bandwidth, i.e. $d_\lambda = N_\nu\Delta\lambda/\lambda_c$. Then

$$\begin{aligned}\Delta\phi_i - \Delta\phi_c &= \left(\frac{\left[\lambda_c + (j-1-\frac{1}{2}N_\nu)\Delta\lambda\right]}{\lambda_c} - 1\right)\Delta\phi_c & (5.14)\\ &= \frac{(j-1-\frac{1}{2}N_\nu)\Delta\lambda}{\lambda_c}\Delta\phi_c & (5.15)\\ &= \frac{(j-1-\frac{1}{2}N_\nu)d_\lambda}{N_\nu}\Delta\phi_c & (5.16)\\ &= \left[\frac{(j-1)}{N_\nu} - \frac{1}{2}\right]d_\lambda\Delta\phi_c & (5.17)\end{aligned}$$

This expression for the difference in phase between channels, $\Delta\phi_{j,c} = \Delta\phi_j - \Delta\phi_c$, is precisely the relationship used in the simulation, where $\Delta\phi_c$ is the given screen phase. Notice that this equation is only a function of simulation parameters and that there is only *relative* wavelength dependence.

We now have an expression for the phase we need to subtract, $\Delta\phi_{j,c}$, to dedisperse the waves *immediately* upon exiting the screen. But how do we dedisperse after the waves have propagated from the screen to the observer? Complicated interference occurs if the phase is corrugated, so it is not necessarily simple. To a good approximation, anything outside of the refractive scale does not contribute to the phase[16]. Thus, we can approximate the phase of the center spectral channel, $\Delta\phi_c$, as the phase of the original screen *averaged over the refractive scale*. So the phase to be subtracted *at the observer* is

$$\Delta\phi_{j,c} = \left[\frac{(j-1)}{N_\nu} - \frac{1}{2}\right]d_\lambda\Delta\phi_{c,\text{ avg}}. \tag{5.18}$$

---

[c] When the N_ν plane waves in the simulation are all separated by a constant wavelength $\Delta\lambda$, then for a particular spatial pixel the phase advancement between consecutive plane waves, $\Delta\phi_{j,j\pm1}$, is constant. However, if ΔDM varies spatially, so too does $\Delta\phi$.

In summary, we scale the spatially smoothed phase of the center frequency by a wavelength dependent function

$$\Delta\phi_{j,c} = g(\lambda)\Delta\phi_c, \tag{5.19}$$

where $g(\lambda) = g(j, d_\lambda, N_\nu)$, and then subtract $\Delta\phi_{j,c}$ from the phase of the j^{th} electric field, ϕ_j,

$$\phi'_j = \phi_j - \Delta\phi_{j,c} \tag{5.20}$$

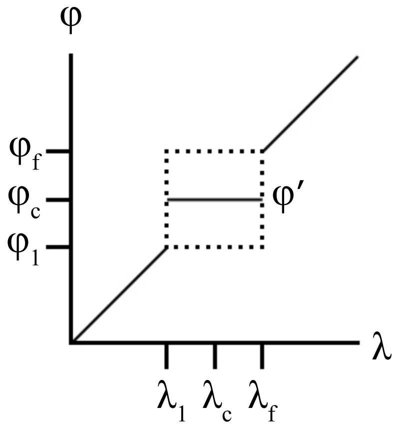

Figure 5.1 – The effect of dispersion is a linear phase ramp in wavelength. Perfect dedispersion removes the wavelength dependence, as in the interval $[\lambda_1, \lambda_f]$.

Notice that we only concern ourselves with relative phase, $\Delta\phi_{j,c}$. Figure 5.1 is a plot of phase as a function of wavelength, where the dedispersed phase is constant across the band at a value of ϕ_c, as Eq. 5.18 dictates. However, the height of the horizontal line can be any arbitrary value of ϕ because a constant phase offset in no way affects the timing information.

$$\begin{aligned} e^{-i[c_1\phi(\lambda)+c_2]} &= e^{-ic_1\phi(\lambda)}e^{-ic_2} && (5.21)\\ &= c_3e^{-ic_1\phi(\lambda)} && (5.22) \end{aligned}$$

The Fourier Transform of an arbitrary scaled function is

$$c_3H(\nu) \leftrightharpoons c_3h(t). \tag{5.23}$$

A constant phase offset changes the amplitude of the function's transform and nothing more.

5.2 Dedispersion Results

A set of five simulations were run to compare a series of impulse responses from dispersed and dedispersed data. In all five runs, dedispersion drastically reduced wander between the

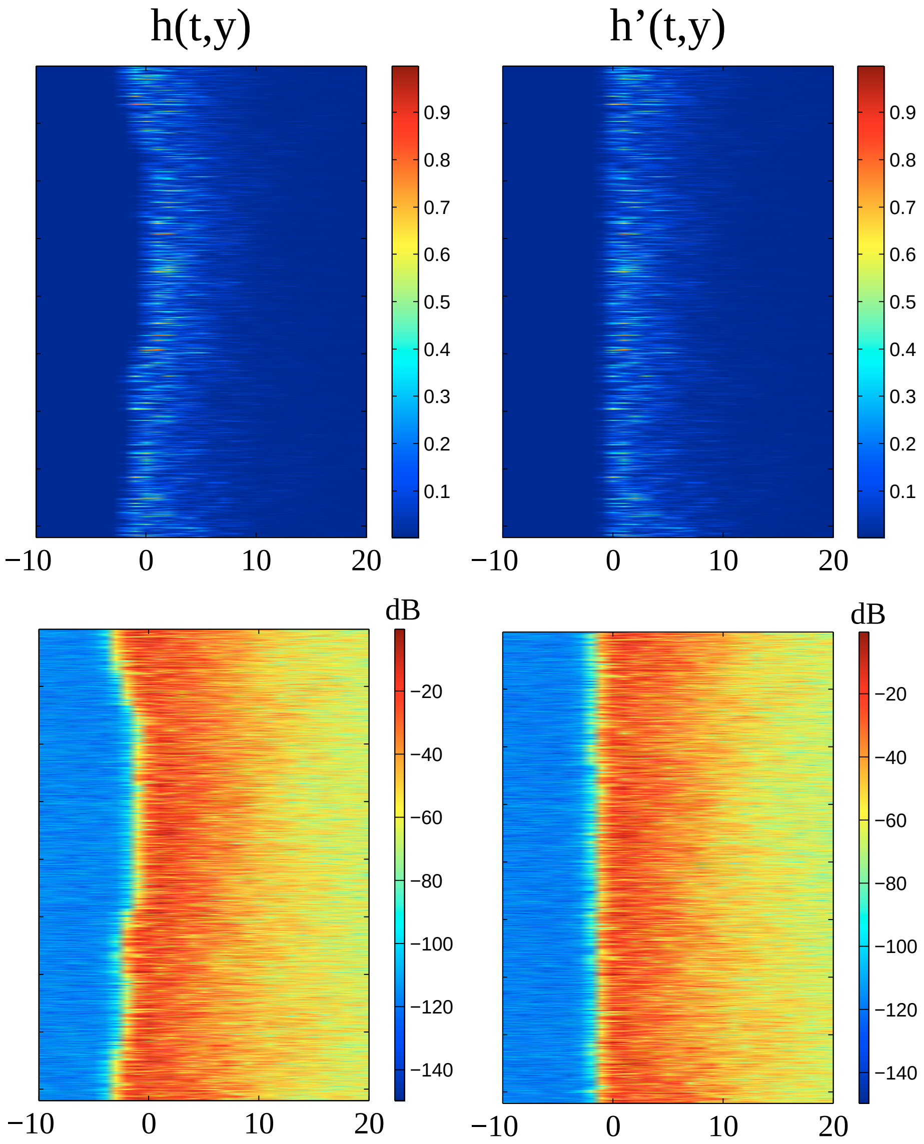

Figure 5.2 – A row of individual impulse responses from Run 1, both dispersed (LEFT) and dedispersed (RIGHT) in linear (TOP) and logarithmic (BOTTOM) displays. Pixel numbers representing delay are displayed on the x-axis and the y-axis is a spatial cut through the observer plane, i.e. $h(t, y)$. The wander is visible in the dispersed impulse response, even in this modest scattering where $m_B^2 = 50$.

leading edge of the Impulse Responses (see Fig. 5.2), and thus reduced the variance in Γ_h. The simulation parameters and resulting centroid standard deviations are listed in Table 5.1.

Run	m_B^2	s_d	s_r	τ_{scatt}	σ_Γ	σ'_Γ
1	50	1.0	110	1.2	1.22	0.224
2	100	0.68	170	2.7	1.66	0.334
3	250	0.39	300	8.2	2.51	0.555
4	500	0.26	460	19	3.38	0.710
5	1000	0.17	690	43	4.68	0.767

Table 5.1 – The values of s_d, s_r, τ_{scatt}, σ_Γ, and σ'_Γ are given in pixels/samples. For all runs $N = 4096$, $N_\nu = 512$, $s_F = 1$, $d_\lambda = 0.05$, and $dx = 0.08$. N^2 is the total number of spatial pixels and dx is the spatial step size relative to s_F.

First-order dedispersion of the simulation shows that the variance of Γ_h can be significantly reduced, but that there is residual variation due to scattering and higher-order dispersion delays (Table 5.1, which we expect because the impulse response width varies. Motivated by the $t_0\tau$ Model, we can decompose Γ_h into an Effective Dispersive Delay, $\widehat{t}_0$, and an Effective Scattering Delay, $\widehat{\tau}$. We show how these quantities are correlated (which is useful for the Statistical Correction in section 4.3) and further suggest what may account for variation in Γ_h beyond $\widehat{t}_0$ and $\widehat{\tau}$.

The $t_0\tau$ Model is not perfectly applicable to the simulation because the individual impulse responses exhibit finite sampling error and are not well-defined by a decaying exponential. However, once the data are dedispersed, the leading edges of the impulse responses tend to align (because first-order dedispersion removes a time shift) and the ensemble-average impulse response, $\langle h \rangle$, becomes a smooth decaying exponential with a finite rise time (see Fig. 5.3). Thus when we dedisperse and average the impulse response over the refractive scale, it is reasonable to use the $t_0\tau$ Model as an approximation.

The centroid of the ACF of the Impulse Response, Γ_R, will clearly serve as τ. In the $t_0\tau$ Model, τ is unaffected by dedispersion, $\tau' = \tau$, and we can see in Figure 5.4 that Γ_R (displayed as $\widehat{\tau}$) is identical in both the dispersed and dedispersed data, $\Gamma'_R = \Gamma_R$. More accurately, $\rho(\Gamma'_R, \Gamma_R) = 0.9993$, therefore it is a very good approximation to say that dedispersion does not change the *shape* of the Impulse Response.

A functional relationship between Γ'_h and Γ_R is predicted by the $t_0\tau$ Model in Eq. 5.10. Since the centroid of the dedispersed Impulse Response, Γ'_h is reasonably correlated with the centroid of the ACF of the Impulse Response, Γ_R, we define an *effective* scattering delay

$$\widehat{\tau} \equiv \Gamma_R, \tag{5.24}$$

which displays all the properties of τ in the $t_0\tau$ Model except that it is not perfectly correlated with Γ'_h (see Table 5.2).

Even when dedispersed, the ensemble-average impulse response does not have a sharp leading edge, which makes it difficult to define a quantity that will serve as t_0 in the $t_0\tau$ Model. An unlikely quantity, the TTA timing point of the impulse response with respect to the ensemble-average impulse response[d], $\Delta t(h, \langle h\rangle)$, was found to display the properties of an offset t_0 when used in conjunction with Γ_R. Specifically, since $\Gamma_h = t_0 + \tau$ in the $t_0\tau$ Model,

$$\Gamma_h = \Delta t(h, \langle h\rangle) + \Gamma_R, \tag{5.25}$$

in both the dispersed and dedispersed data. This result can be seen by the strong correlations in Table 5.2 and the associated figures (displayed as $\widehat{t_0}$). Therefore, we would expect that

$$\Delta t(h', \langle h'\rangle) = 0 \tag{5.26}$$

since first-order dedispersion removes time offsets. But we must be cautious because $\Delta t(h', \langle h'\rangle)$ does *not* vanish (see Fig. 5.4). Let us define an *effective* dispersive delay

$$\widehat{t_0} \equiv \Delta t(h, \langle h\rangle), \tag{5.27}$$

which displays all the properties of t_0 except that it is not fully removed by first-order dedispersion, $\widetilde{t_0'} \neq 0$. This is analyzed more closely in Appendix B.

The centroid of the Impulse Response is *the* ISM delay; constructing $\widehat{t_0}$ and $\widehat{\tau}$ is a way to break the centroid into its components (Dispersive and Scattering delays). We are "peeling the onion" of the centroid to determine how it is constituted. If $\widehat{t_0}$ and $\widehat{\tau}$ were the only components, then

$$\Gamma_h - \left(\widehat{t_0} + \widehat{\tau}\right) = 0. \tag{5.28}$$

However, we find that this subtraction does not yield zero – there is residual variation in the centroid beyond these two terms. The spatial gradient of the smoothed phase screen has some correlation with the residual variation (see Fig. 5.5), but it cannot be the whole story. The next layer of the onion is unknown.

Correlation	Dispersed	Dedispersed	Plot Location
$\rho(\widehat{\tau}, \widehat{t_0})$	-0.194	0.612	Fig. 5.6 (Left)
$\rho(\Gamma_h, \widehat{\tau})$	-0.128	0.872	Fig. 5.6 (Right)
$\rho(\Gamma_h, \widehat{t_0})$	0.998	0.917	Fig. 5.7 (Red)
$\rho(\Gamma_h, \widehat{t_0} + \widehat{\tau})$	0.999	0.998	Fig. 5.7 (Blue)

Table 5.2 – Various correlations between $\widehat{\tau}$, $\widehat{t_0}$, and Γ_h for both dispersed and dedispersed simulation data as shown in Figures 5.6 and 5.7.

---

[d] This must not be confused with the TTA timing point of the observed pulse with respect to the intrinsic pulse, $\Delta t(p, i) = \Gamma_h$.

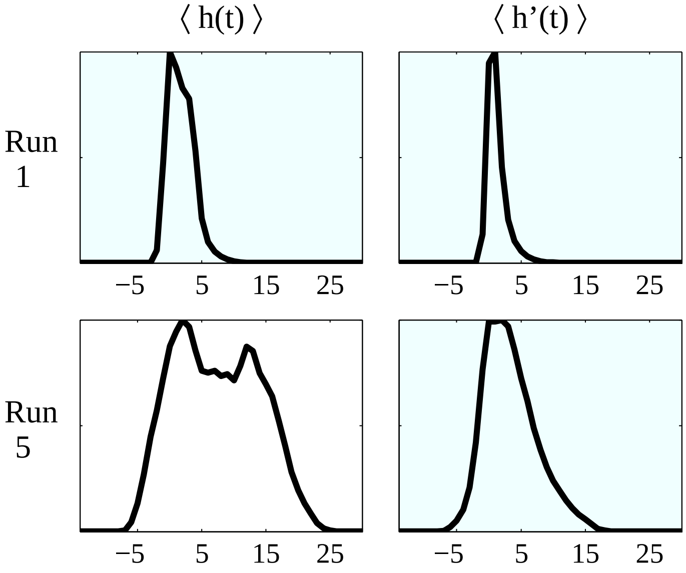

Figure 5.3 – Dispersed (LEFT) and dedispersed (RIGHT) ensemble-average impulse responses. Pixel numbers representing delay are displayed on the x-axis.

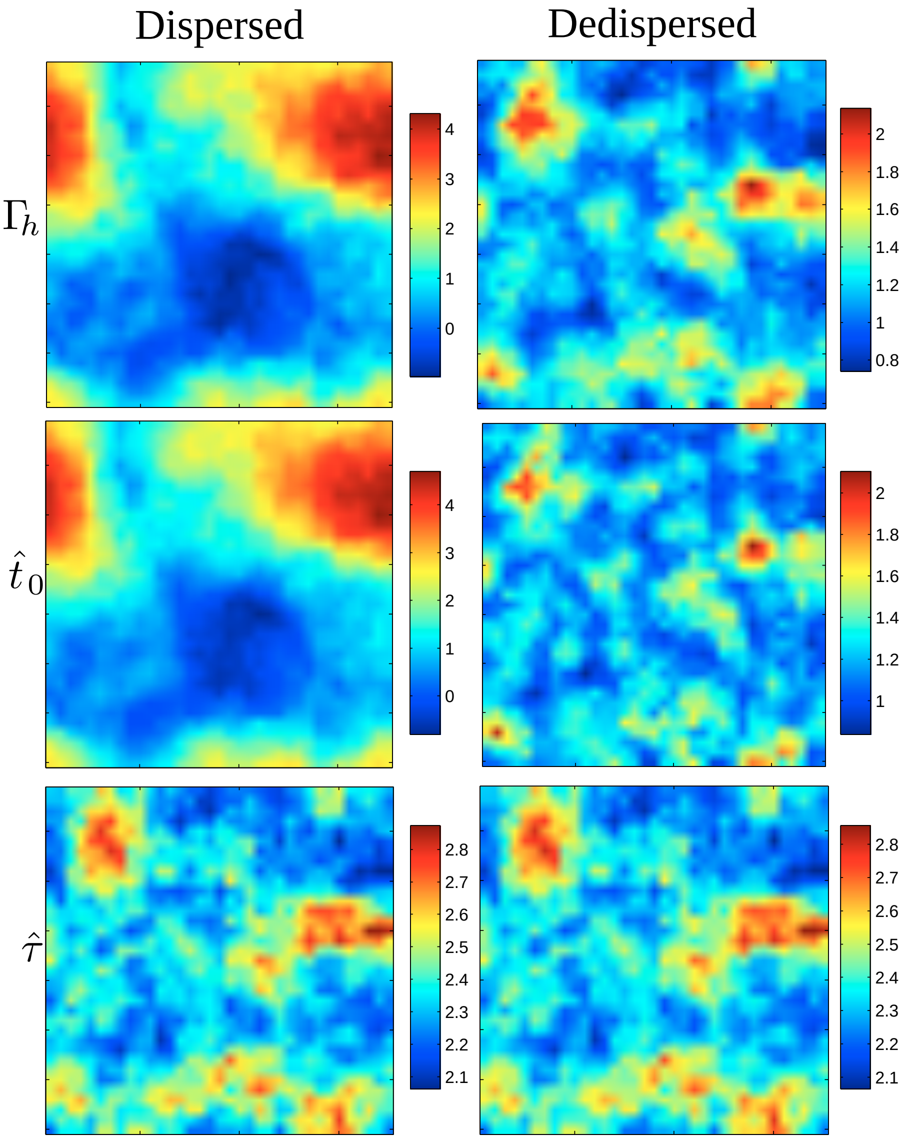

Figure 5.4 – Γ_h, $\widehat{t}_0$, and $\widehat{\tau}$ are imaged as a function of spatial pixel (averaged over the refractive scale) for both dispersed and dedispersed data.

5.3 The Parkes PTA and Dispersion Measure Variations

Quantities that cannot be determined observationally are accessible in the simulation: the electric field, the physical scattering screen, and anything derivable from those two. While such omniscience allows us to wholly understand the simulation's realization of interstellar propagation, it is useful to feign ignorance to see what can be accomplished using only information that is accessible to observers.

The Parkes Pulsar Timing Array (PPTA) group uses measurements at two wavelengths, 50 and 10 cm, to determine dispersion measure fluctuations (ΔDM) as a function of time[42]. They do this by fitting for λ^2 dependence in the timing residuals for each timing point,

$$\begin{aligned}\Delta t_2 - \Delta t_1 &\propto \left(\frac{1}{\nu_2^2} - \frac{1}{\nu_1^2}\right)\Delta\mathrm{DM} && (5.29)\\ \Delta\mathrm{DM} &\propto \left(\frac{\Delta t_2 - \Delta t_1}{\nu_2^{-2} - \nu_1^{-2}}\right) && (5.30)\end{aligned}$$

since $\Delta t \propto \nu^{-2}\Delta\mathrm{DM}$. The complex impulse response provides all the information necessary to determine the effects of interstellar propagation, but it is not an observable, so we discard it to mimic the conditions of the PPTA observations.

The simulation is inherently achromatic – it is not run at a specific frequency. Instead, all calculations are based on the Fresnel scale, s_F. Since the Fresnel scale is proportional to the square root of the observing wavelength, we can simulate observations at two different wavelengths by using two different s_F. Therefore, to mimic the PPTA observations at $\lambda_1 =$ 10 cm and $\lambda_2 = 50$ cm, the Fresnel scales must be related to each other by $s_{F,2} = \sqrt{5}s_{F,1}$. All simulation parameters that have a wavelength dependence must be similarly scaled:

Quantity	λ Scaling
s_F	$\lambda^{1/2}$
d_λ	λ^{-1}
m_B^2	$\lambda^{17/6}$
s_d	$\lambda^{-6/5}$
s_r	$\lambda^{6/5}$

Table 5.3 – For this simulation, Kolmogorov turbulence is used, i.e. $\alpha = 5/3$. The wavelength scalings of m_B^2, s_d, and s_r depend explicitly on α.

The m_B^2 scaling occurs because[20]

$$m_B^2 \propto \left(\frac{s_F}{s_d}\right)^{5/3}. \tag{5.31}$$

Thus, we have the relationships necessary to simulate multi-frequency observations.

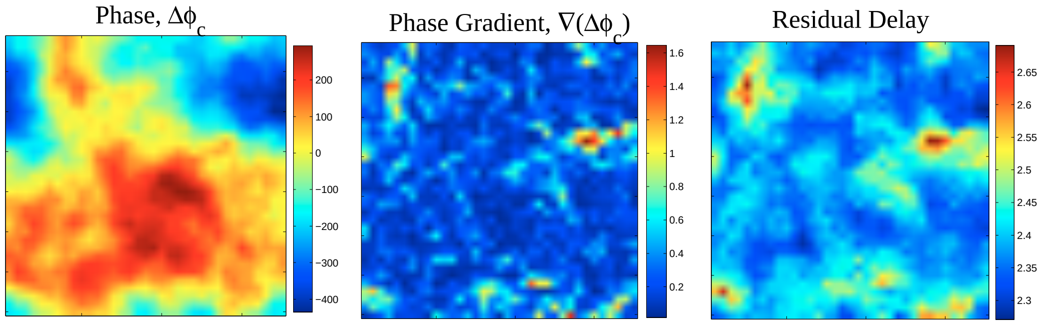

Figure 5.5 – The phase screen (LEFT), its gradient squared (MIDDLE), and the residual delay after $\left(\widehat{t}_0 + \widehat{\tau}\right)$ is subtracted from Γ_h (RIGHT) are imaged as a function of spatial pixel (averaged over the refractive scale). Components of the centroid not accounted for by $\widehat{t}_0$ or $\widehat{\tau}$ may include delay due to the refractive scattering angle (the phase gradient squared).

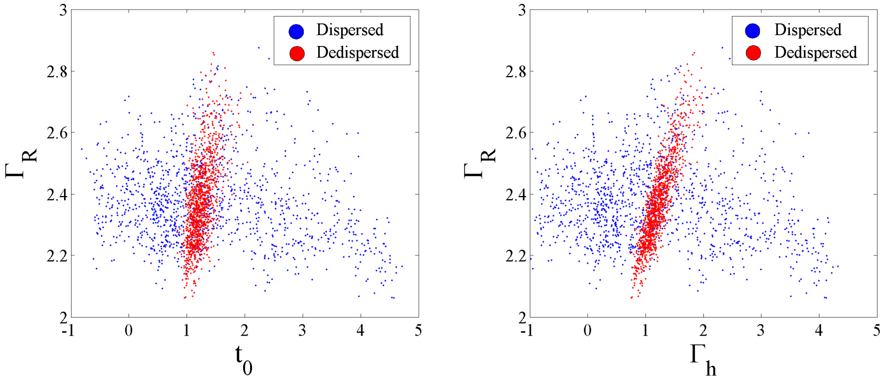

Figure 5.6 – Scatter plot of $\widehat{\tau}$ against $\widehat{t}_0$ (LEFT) and Γ_h (RIGHT), where the axes display time sample number. The correlations significantly increase when the data is dedispersed.

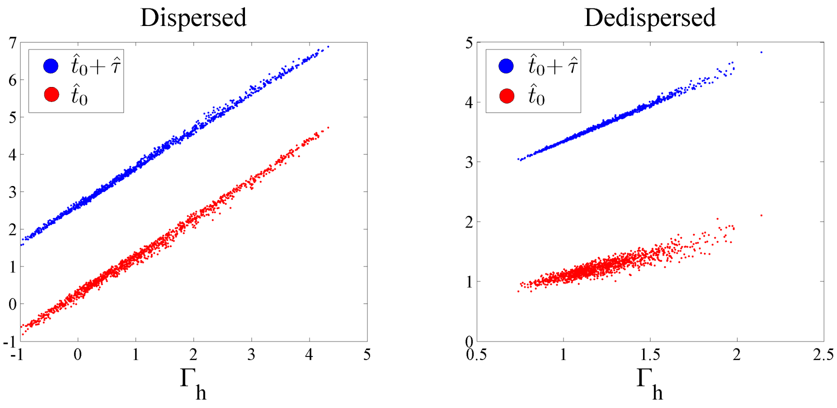

Figure 5.7 – Scatter plot of Γ_h against $\widehat{t}_0$ (RED) and $\widehat{t}_0 + \widehat{\tau}$ (BLUE), where the axes display time sample number. For both dispersed and dedispersed data, the latter is nearly unity.

We calculate the timing residuals the way an observer might, by using the Talyor Timing Algorithm (TTA) on the observed pulse profiles, $p(t)$. Since observed pulse profiles are not a simulation output, they are constructed by convolving an intrinsic pulse profile $i(t)$ with the impulse response. However, the timing residuals can be approximated independently of the intrinsic pulse profile (thus making it independent of the pulsar). In §4.1 we showed that if the width of the intrinsic pulse profile is much greater than the width of the impulse response, then the timing residual (from the TTA) of their convolution is simply the width of the impulse response, or if the impulse response is offset from the origin, its centroid (which is just the sum of width and offset), $\Delta t(p,i) = \Gamma_h$.

Because the simulation is noiseless, we are guaranteed that the timing residuals are entirely a result of interstellar propagation effects. Also, because we are omniscient, we can compare the observational method of ΔDM determination with the ΔDM used in the simulation. Thus we can judge the accuracy of this method in the ideal condition when interstellar propagation effects dominate the timing residuals. We could also comment on the accuracy when interstellar propagation effects are buried in noisy residuals by adding noise to the simulation.

To compare the true ΔDM with the observationally motivated derivation of ΔDM, we need to specify how phase and delay relate to ΔDM. In the mks unit system, they are

$$\begin{aligned} \Delta\mathrm{DM} &= 4\pi\epsilon_0 e^{-2} m_e c\, \frac{\Delta\phi}{\lambda} && (5.32)\\ &= \left(3.8\times 10^{-8}\ \frac{\mathrm{ns}\cdot\mathrm{pc}}{\mathrm{cm}^3\cdot\mathrm{rad}}\right)\nu_{\mathrm{GHz}}\Delta\phi && (5.33)\\ \Delta\mathrm{DM} &= 8\pi^2\epsilon_0 e^{-2} m_e c\, \frac{\Delta t}{\lambda^2} && (5.34)\\ &= \left(2.41\times 10^{2}\ \frac{\mathrm{ns}^2\cdot\mathrm{pc}}{\mathrm{cm}^3\cdot\mathrm{s}}\right)\nu_{\mathrm{GHz}}^2\Delta t && (5.35) \end{aligned}$$

where $\Delta\phi$ is in radians, Δt is in seconds, and ΔDM is in pc/cm^3. The simulation provides $\Delta\phi$ in radians and Δt in time samples, which can be converted to physical time units by multiplying the sample number by twice the observational bandwidth, B, in Hz,

$$t_{\mathrm{physical}} = 2B\, t_{\mathrm{sample}}. \quad (5.36)$$

Once phase and delay are transformed, a simple subtraction of the resulting ΔDM shows how well the two determinations compare.

The simulation was run with the parameters in Table 5.4. The determinations are nearly identical when the scattering strength (m_B^2) is small – the pulsar beam is weakly scattered, illuminating a small region of the scattering screen. But, *so far*, they are incomparable when m_B^2 is large, which is the case for most pulsars – the beam is strongly scattered, and a large region of the scattering screen contributes to the observed electric field phase. Basically, this is a function of the refractive scale increasing with wavelength (see Table 5.3). Figures 5.8 and 5.9 show the results of these simulations.

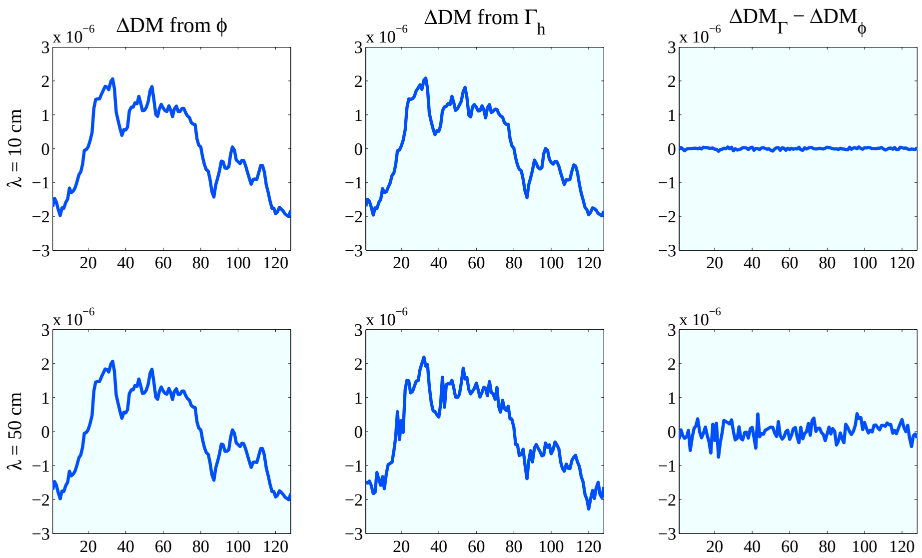

Figure 5.8 – ΔDM determination in weak scattering. For $\lambda = 10$ cm, $m_B^2 \approx 0.1$, and for $\lambda = 50$ cm, $m_B^2 = 10$. The units of DM are pc/cm^3.

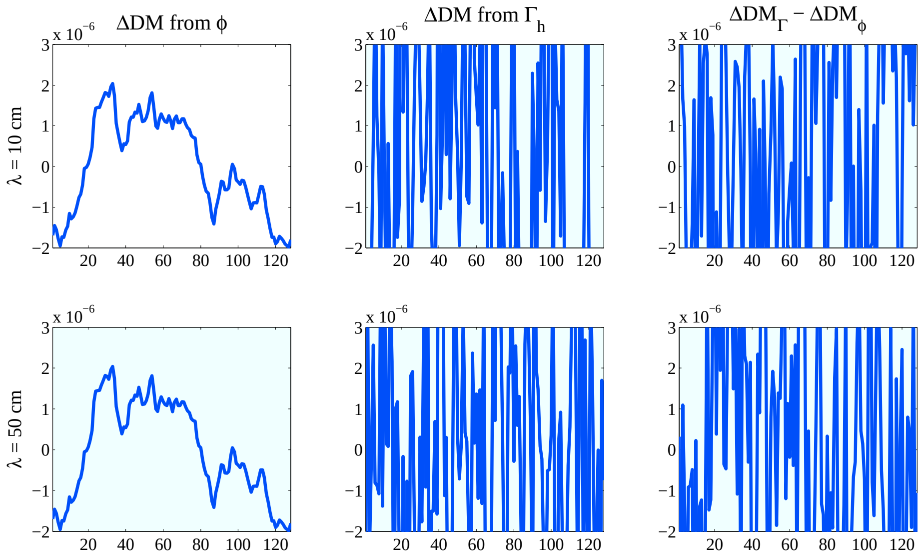

Figure 5.9 – ΔDM determination in strong scattering. For $\lambda = 10$ cm, $m_B^2 = 10$, and for $\lambda = 50$ cm, $m_B^2 \approx 1000$. The units of DM are pc/cm^3.

Regime	Weak	Scattering	Strong	Scattering
λ	10 cm	50 cm	10 cm	50 cm
m_B^2	0.105	10	10	956
s_F	0.45	1	1	2.24
d_λ	0.083	0.094	0.083	0.094
dx	0.07	0.07	0.01	0.01
s_d	6.4	3.1	21.5	3.12
s_r	6.4	50	350	12000
τ_{scatt}	0.01	0.32	0.28	77

Table 5.4 – Simulation parameters used for the ΔDM comparison. The values of s_d, s_r, and τ_{scatt} are given in pixels/samples.

We conclude that the formula specifying how delay relates to ΔDM, Eq. 5.2, accurately describes interstellar propagation effects most precisely when the scattering screen is a uniform, flat slab of ions (the limiting case of $m_B^2 = 0$). It *only* accounts for frequency effects, dispersion – not the effects of a spatially varying dispersion measure, which causes scattering (refraction and diffraction). It is not yet clear how quickly this observational (PPTA) method breaks down as scattering strength increases, or if there is a way to improve it.

While the agreement between the observational and true DM variation in Figure 5.8 is remarkably good in the case of $m_B^2 = 0.1$ for $\lambda = 10$ cm, we must consider the scale of the variation. The best techniques can measure a ΔDM as small as 10^{-3} pc/cm^3, and a typical observed ΔDM is 10^{-2} pc/cm^3 over a one year period[42]. Therefore, the small ΔDM for $m_B^2 = 0.1$ on the order of 10^{-6} pc/cm^3 is unmeasurable and unrealistic. But when we increase the scattering strength, the observationally determined ΔDM is not a good measure of the true ΔDM– it is difficult to accurately determine the dispersion measure. We will continue to refine our analysis in order to improve ΔDM determinations in stronger scattering regimes.

Chapter 6

Future Fun

I am glad that there is still much more to do with respect to this project. For anyone who might participate in this research, there is no future work. There is only future fun.

Much fun remains to be had before the algorithm presented in §3.1 can be used in pulsar timing routines. Most pulsars in the PPTA, for instance, are millisecond pulsars, which are recycled (spun-up to millisecond periods, possibly through accretion) and extremely stable. Our analysis is of PSR B1737+13, a normal pulsar with a period of 0.803 seconds[56;57] whose scintillation behavior could be different than that of millisecond pulsars – we don't know. Using the algorithm on archived pulsar timing data where spectra were taken will indicate whether the current algorithm is appropriate and whether such spectral analysis is even possible.

The algorithm presented herein provides a post-detection correction for interstellar delays. However, we would not be physicists if we didn't want to *predict* delays. Measuring the change in delay as arclets translate along scintillation arcs will determine whether or not scattering delays can be predicted with our technique. Such a study would require observations spaced out to appropriately resolve the refractive scale. B1737 is a good candidate for study because its scintillation is well-suited for our technique (it was *made* for B1737!), and the conclusion about the predictive power of our technique would be unambiguous.

Though not directly applicable to pulsar timing, scintillation observations can be made to track the distribution of arclet progenitors – compact, overdense structures – on the sky. A map of their spatial distribution might provide insight into the physical processes in the ISM that are creating these structures. Ultimately, a better understanding of the ISM will help us correct for interstellar propagation effects.

There is fun ahead on the theoretical and simulation fronts as well. The Coles wave-propagation simulation does not have the ingredients to replicate all the observed features in the Secondary Spectrum. In particular, arclets are missing from the simulation, and they need to be found. One project in progress searches for arclets by masking the scattering screen to simulate spatially compact structures in the ISM. Another possible investigation is the use of multiple scattering screens to simulate an extended medium.

We have made several approximations in our theoretical analysis of the effect of propagation delays on TTA timing points. One is the $t_0\tau$ Model, another is a constraint of the relative widths of the impulse response and intrinsic pulse. While these approximations have been quite useful and have led to important insights, there is the chance that they could be obscuring some important subtleties. By working directly with the TTA cross-correlation equation and a more general expression for the impulse response, we may be able to *exactly* describe the effect of interstellar propagation on timing residuals.

These forays do not even begin to quantify the amount of "low-hanging fruit" on the trees of pulsar scintillation spectra and GW astrophysics. With the possibility of GW detections in the near future from LIGO or LISA, gravitational-wave astrophysics is burgeoning. We can truly propel the science by using pulsar timing to its fullest in the meantime, and that will require us to use everything we know about pulsars and the ISM.

Onwards and upwards.

Appendix A

On Dedispersion

The dispersion relation for electromagnetic waves is,

$$k(\omega) = \frac{\omega}{c} n, \tag{A.1}$$

where n is the index of refraction of the propagation medium. In a vacuum, it's the familiar $k = \omega/c$ because the index of refraction is $n = 1$. When that wave enters a *tenuous, cold plasma*, the dispersion relation becomes

$$k(\omega) = \frac{\omega}{c}\sqrt{1 - \frac{\omega_p^2}{\omega^2}}, \tag{A.2}$$

where ω is the wave frequency[a] and ω_p is the plasma frequency,

$$\omega_p = \sqrt{\frac{e^2 n_e}{m_e \epsilon_0}}. \tag{A.3}$$

in mks units. Notice that an index of refraction $n < 1$ is implied for this medium.

From the dispersion relation, the following important quantities are derivable. The group velocity (the speed at which a wave packet propagates through the medium) is

$$v_g(\omega) = \frac{\partial \omega}{\partial k}. \tag{A.4}$$

Group delay, the total propagation time of a wave packet, is given by

$$\begin{aligned} t_g &= \int_0^D \frac{1}{v_g}\, d\ell && \text{(A.5)} \\ &= \int_0^D \frac{\partial k}{\partial \omega}\, d\ell && \text{(A.6)} \end{aligned}$$

---

[a] We have used ν for frequency in the body of the thesis. The switch to $\omega = 2\pi\nu$ was made here to simplify the expressions.

And the "group phase" is given by

$$\begin{aligned}
\phi_g(\omega) &= \int t_g \, d\omega && \text{(A.7)}\\
&= \int_0^D \int \frac{\partial k}{\partial \omega} d\omega \, d\ell && \text{(A.8)}\\
&= \int_0^D k(\omega) \, d\ell && \text{(A.9)}
\end{aligned}$$

Finally, the transfer function (the spectral filter that characterizes the medium's effect on a propagating wave) is

$$\begin{aligned}
H(\omega) &= \exp\left[-i \int_0^D k(\omega) \, d\ell\right] && \text{(A.10)}\\
&= \exp\left[-i\phi_g(\omega)\right] && \text{(A.11)}
\end{aligned}$$

This is as far as we can go without introducing the approximation for when $\omega_p \ll \omega$, which is *always* true in the ISM because the plasma frequency $\omega_p \propto$ kHz, while the observation frequency $\omega \propto$ MHz or GHz. Using the binomial expansion, the group delay can be reduced to

$$\begin{aligned}
t_g &= \frac{1}{c} \int_0^D \left[1 - \frac{\omega_p^2}{\omega^2}\right]^{-1/2} d\ell && \text{(A.12)}\\
&\approx \frac{1}{c} \int_0^D \left[1 + \frac{\omega_p^2}{2\omega^2}\right] d\ell && \text{(A.13)}\\
&\approx \frac{1}{c} \left[D + \frac{e^2}{2m_e\epsilon_0 \, \omega^2} \int_0^D n_e \, d\ell\right] && \text{(A.14)}\\
&\approx \frac{D}{c} + \frac{e^2 \mathrm{DM}}{2m_e\epsilon_0 c \, \omega^2} && \text{(A.15)}
\end{aligned}$$

and the group phase can be reduced to

$$\begin{aligned}
\phi_g &= \int t_g \, d\omega && \text{(A.16)}\\
&\approx \int \left(\frac{D}{c} + \frac{e^2 \mathrm{DM}}{2m_e\epsilon_0 c \, \omega^2}\right) d\omega && \text{(A.17)}\\
&\approx \frac{D}{c}\omega - \frac{e^2 \mathrm{DM}}{2m_e\epsilon_0 c \, \omega} && \text{(A.18)}
\end{aligned}$$

Thus, our ultimate equation for the transfer function relies only on the assumption of cold, tenuous plasma with a plasma frequency $\omega_p \ll \omega$.

$$\begin{aligned}
H(\omega) &\approx exp\left[-i\omega\frac{D}{c} + i\frac{e^2 \mathrm{DM}}{2m_e\epsilon_0 c \, \omega}\right] && \text{(A.19)}\\
H(\lambda) &\approx exp\left[-i\frac{2\pi D}{\lambda} + i\lambda\frac{e^2 \mathrm{DM}}{4\pi m_e\epsilon_0 c^2}\right] && \text{(A.20)}
\end{aligned}$$

But when we also restrict the bandwidth to be much less than the frequency, the arguments of both exponentials are essentially linear in the independent variable. When ϕ_g is expanded in a Taylor series, then the terms are accounting for the degree to which $1/\omega$ deviates from $-\omega$.

The impulse response of the medium is the power spectrum of the transfer function,

$$h(t) = |\widetilde{H}(f_\omega)|^2. \tag{A.21}$$

When the phase of the transfer function is linear in ω, then the phase contribution from DM induces a time shift in the impulse response with respect to an undeviated wave.

Appendix B

Analysis of $\widehat{t_0}$

In this appendix we analyze the behavior of a quantity that was introduced in section 5.2 to describe the time offset behavior of an Impulse Response that does not have a precise time offset. Whereas t_0 is the offset in the $t_0\tau$ Model, we use an effective offset (Dispersion Delay)

$$\widehat{t_0} \equiv \Delta t(h, \langle h \rangle) \tag{B.1}$$

in the Coles simulation data. We also introduced an effective width (Scattering Delay)

$$\widehat{\tau} \equiv \Gamma_R. \tag{B.2}$$

The similarities between the $t_0\tau$ and Effective Delays are

$$\begin{aligned} \Gamma_h &= t_0 + \tau && \text{(B.3)} \\ \Gamma_h &= \widehat{t_0} + \widehat{\tau} && \text{(B.4)} \end{aligned}$$

The differences are

$$\begin{aligned} \widehat{\tau} &\neq \Gamma'_h && \text{(B.5)} \\ \widehat{t_0'} &\neq 0 && \text{(B.6)} \end{aligned}$$

where a primed symbol refers to a dedispersed quantity.

A simple thought experiment helps to probe the meaning of these effective delays. Consider a set of $t_0\tau$ Impulse Responses with a set of t_0 and τ. First, let τ be constant and let t_0 vary.

$$h(t, y) = H(t - t_0(y)) \exp\left[(t - t_0(y))/\tau\right] \tag{B.7}$$

We know analytically that $\widehat{\tau} = \tau$ since this is the $t_0\tau$ Model. Because the ensemble-average Impulse Response, $\langle h \rangle$, is broadened symmetrically by the range of t_0, we find numerically[a] that $\widehat{t_0} = t_0$ (see Fig. B.1).

---

[a] The numerical analysis used 100 impulse responses whose offsets t_0 and widths τ were Gaussian random deviates.

Second, let τ vary and let t_0 be constant.

$$h(t, y) = H(t - t_0) \exp\left[(t - t_0)/\tau(y)\right] \tag{B.8}$$

The ensemble-average Impulse Response, $\langle h \rangle$, will assume a width that is the average of τ, but it may not strictly be a decaying exponential. We find numerically that $\widehat{t}_0 \approx 0$ (see Fig. B.2), but that it has a functional relationship with τ.

Finally, let both τ and t_0 vary. We find numerically that $\Gamma_h = \widehat{t}_0 + \tau$, but no other relationships can be found (see Figs. B.3 and B.4).

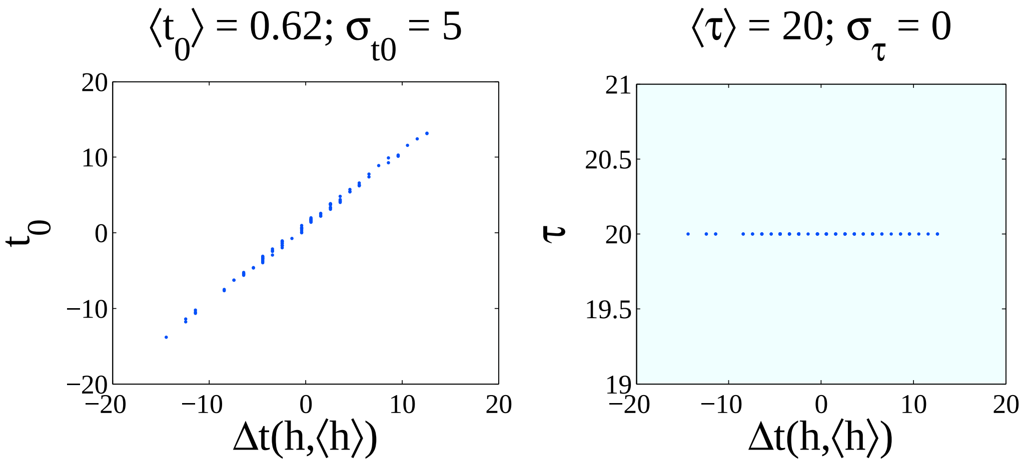

Figure B.1 – The effective offset $\widehat{t}_0$ correlates well with t_0 when τ is constant. There is almost a functional equivalence between the two.

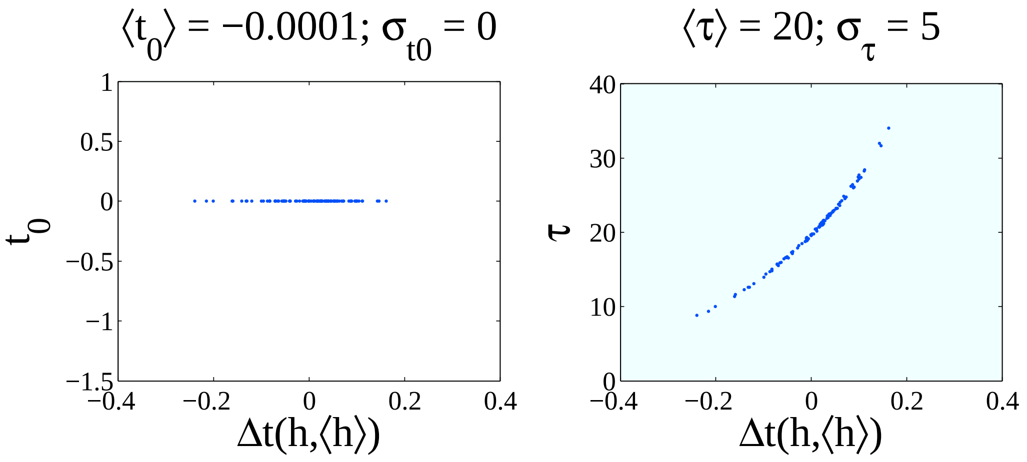

Figure B.2 – The effective offset $\widehat{t}_0$ is approximately zero when t_0 is constant. However, there is an unexpected almost quadratic relationship between $\widehat{t}_0$ and τ. In a timing sense this is inconsequential because the variation in τ is orders of magnitude larger than the variation in $\widehat{t}_0$.

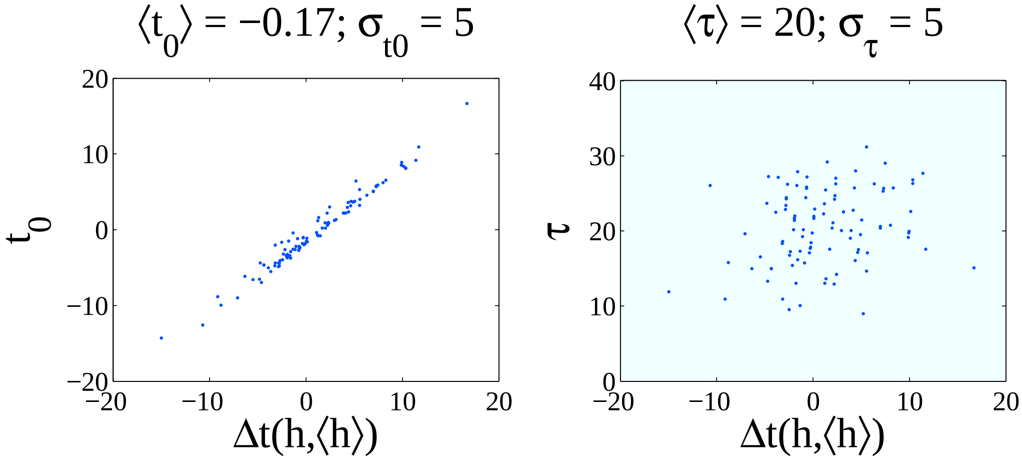

Figure B.3 – When both t_0 and τ vary (with the same standard deviation), the effective offset $\widehat{t_0}$ is *almost* equivalent to t_0 and has no correlation with τ.

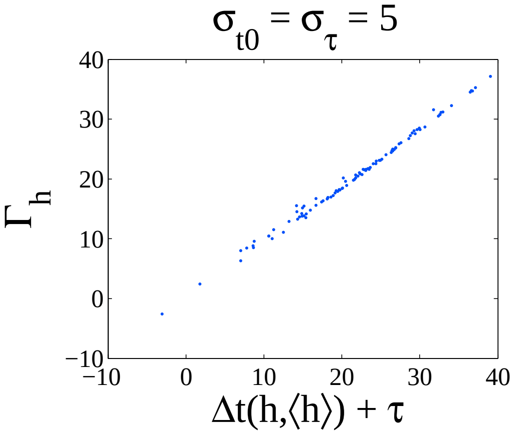

Figure B.4 – The effective offset $\widehat{t_0}$ added to τ is an almost functional equivalence regardless of the standard deviation of t_0 and τ. This is predicted by Eq. B.4, noting that when using the $t_0\tau$ Model, $\widehat{\tau} = \tau$.

Appendix C

Glossary

Acronym	Terminology
ACF	Autocorrelation Function
AU	Astronomical Unit
BH	Black Hole
BW	Bandwidth
DFT	Discrete Fourier Transform
DM	Dispersion Measure
FT	Fourier Transform
GW	Gravitational Wave
HWHM	Half-width at Half-maximum
ISM	Interstellar Medium
LIGO	Laser Interferometer Gravitational-wave Observatory
LISA	Laser Interferometer Space Antenna
PPTA	Parkes Pulsar Timing Array
PTA	Pulsar Timing Array
SNR	Signal to Noise Ratio
TOA	Time Of Arrival
TTA	Taylor Timing Algorithm
WAPP	Wideband Arecibo Pulsar Processor

Symbol	Generalized Expressions
R_X	ACF of X
P_X	Power Spectrum of X
Γ_X	Centroid of X
σ_X^2	Variance of X
σ_X	Standard Deviation of X
$\sigma_{X,Y}$	Covariance of X and Y
$\rho(X,Y)$	Correlation coefficient between X and Y
$\Delta t(\mathrm{X,Y})$	TTA timing point of X with respect to Y
$\widetilde{X}$	Fourier Transform of X

Symbol	Specific Expressions
$i(t)$	Intrinsic Pulse Profile
$p(t)$	Observed Pulse Profile
$h(t)$	Impulse Response
Δt	Timing Residual
$R_h(t)$	ACF of the Impulse Response
Γ_h	Centroid of the Impulse Response
$\Gamma_{R_h}(T)$	Cumulative Delay
Γ_{R_h}, Γ_R	Centroid of the ACF of the Impulse Response
τ	Scattering Delay, Width of the $t_0\tau$ Impulse Response and its ACF
t_0	Dispersion Delay, Offset of the $t_0\tau$ Impulse Response
$E(t,\nu)$	Electric Field
$I(t,\nu)$	Dynamic Spectrum
$R_I(t,\nu)$	ACF of the Dynamic Spectrum
$\Delta\nu_d$	Diffractive Bandwidth
Δt_d	Diffractive Timescale
τ_{scatt}	Scattering Delay, determined by $\Delta\nu_d$
s_F	Fresnel Scale
s_d	Diffractive/Coherence Scale
s_r	Refractive Scale
d_λ	Fractional Bandwidth
m_B^2	Square Born Scattering Index
N_ν	Number of Frequency Channels
$\widehat{\tau}$	Effective Scattering Delay, Coles simulation data analysis
$\widehat{t}_0$	Effective Dispersion Delay, Coles simulation data analysis
$H(t-t_0)$	Heaviside Step Function
$\leftrightharpoons$	Fourier Transform

Appendix D

Code

Many thousands of lines of code have been written (in MATLAB) for processing the Coles simulation output data and for processing the B1737 data. The hearts of these two processing scripts are included here. For the Coles simulation output processing:

```
%%%%%%%%%%%%%%%%%%%%%%%% Last Updated: 20 Mar. 2007 %%%%%%%%%%%%%%%%%%%%%%%
%
%************************* HELP FILE INFORMATION *************************%
% [h(y,t), S(y,t)] = distfn_ProcessEfield(Vars)
%
% The observer plane (complex E-field) is stored in N_f arrays.
%
% This is a procedure to take a complex E-field (spatial, spatial) in each
% frequency array and calculate:
%   1. Impulse Response of the screen is the output averaged by a specified
%      method.
%   2. Dynamic spectrum averaged by a specified method.  The UN-WINDOWED
%      E-field is used to create this.
%      To normalize power between the Impulse Response and Dynamic
%      Spectrum, multiply the Dynamic Spectrum by the SQUARED 1-D window
%      (in the spatial dimension) that was used to create the Impulse
%      Response.
%
% Dependent function files:
%   - fn_ReadHeader
%   - fn_Dedisperse
%   - distfn_JobStartup
%*************************************************************************%
```

```
function [h,S] = distfn_ProcessEfield(Vars)

tic
%%%%%%%%%%%%%%% Prepare for Data Import /// Set Variables %%%%%%%%%%%%%%%
%Extract the variables from Vars
Path_Efield = Vars{1};
Path_Header = Vars{2};
Rows = Vars{3};
Pad = Vars{4};
FTfilter = Vars{5};
Precision = Vars{6};
NumNodes = Vars{7};
TaskNum = Vars{8};
RowAvgMat = Vars{9};
ColAvgMat = Vars{10};
Dedisperse = Vars{11};
Phase = Vars{12};
CodeDir = Vars{13};

%Adjust directory settings
cd(CodeDir);
addpath([CodeDir,'../..']);

%Get necessary parameters from the simulation header file
[N_x, N_f] = fn_ReadHeader(Path_Header)

%Specify the particular rows (y) to extract.
RowStart = Rows(1)
RowEnd = Rows(end)

%Two matrices, RowAvgMat/ColAvgMat, are given to every node.  On each row
%of these matrices is a list of spatial pixels that should be averaged.
%This will be done using ColAvgMat for every row, and then each node will
%average the rows with RowAvgMat as best they can.  dist_ProcessEfield will
%average the output of distfn_ProcessEfield together appropriately, since
%there is no guarantee that (because of the particular rows each node will
%get) it will be able to average the rows completely.
%Determine the number of blocks to be averaged together (and how many
%columns each block includes, ColsPerBlock)
[N_ColBlocks, ColsPerBlock] = size(ColAvgMat)
```

```
[N_RowBlocks, RowsPerBlock] = size(RowAvgMat)

%Determine which block of rows RowStart and RowEnd belong to
[RowStart_Block, temp] = find(RowAvgMat == RowStart)
[RowEnd_Block, temp] = find(RowAvgMat == RowEnd)
N_RowBlocks = RowEnd_Block - RowStart_Block + 1
%%%%%%%%%%%%%%%%%%%%%%%%%%%%%%%%%%%%%%%%%%%%%%%%%%%%%%%%%%%%%%%%%%%%%%%%%%%

%****************************** Load Data ******************************%
%Change the frequency order depending on the task number (this decreases
%the nodes simultaneously trying to access the same data).
FreqOrder = circshift((1:N_f)', round((1-TaskNum)*N_f/NumNodes));

%Open the files for reading for each jobTask
for n = 1:N_f
    f = FreqOrder(n);

    %Open each of the N_f input files
    FreqNum = num2str(f);
    while length(FreqNum) < 4
        FreqNum = strcat('0', FreqNum);
    end

    Path_Slice = [Path_Efield, FreqNum, '.2d'];
    FileID(f) = fopen(Path_Slice, 'r');
end
toc

%Create a Fourier Transform filter, if specified
if ~isempty(FTfilter)
    FilterFunction = str2func(FTfilter);
    Filter_FT = repmat(FilterFunction(N_f),[1, N_x])';
end

%Seek to the appropriate starting row of the data (Complex Data)
for n = 1:N_f
    f = FreqOrder(n);
    setRowStart = fseek(FileID(f), 8*(RowStart-1)*N_x, 'bof');
end
```

```
%Initialize the Efield array and the output, h and S
Efield = zeros([N_x, N_f], 'single');
h = zeros([N_RowBlocks*N_ColBlocks, N_f], 'single');
S = zeros([N_RowBlocks*N_ColBlocks, N_f], 'single');
%*********************************************************************%

%***************************** Main Loop *****************************%
%Calculate h and S for each row
Time = toc
for y = RowStart:RowEnd

    for n = 1:N_f
        f = FreqOrder(n);
        %Load one spatial row of the E-field
        EData = fread(FileID(f), [2, N_x], ['*',Precision]);
        Efield(:,f) = EData(1,:) + i*EData(2,:);
    end

    if Dedisperse == 'y'
        %Load one spatial row of the phase screen
        PhaseRow = Phase(y-RowStart+1,:);

        %Perform the phase correction for each (x,f) of this row.
        Vars = {Path_Header, PhaseRow, Efield};
        Efield = fn_Dedisperse(Vars,'prrow');
    end

    ReadTime = toc - Time
    Time = toc;

    %Initialize some quantities
    IR_onerow = zeros(N_ColBlocks,N_f);
    Spect_onerow = zeros(N_ColBlocks,N_f);

    %Determine which row-blocks this row belongs to
    [RowBlock, temp] = find(RowAvgMat == y)
    %Determine the blocks to put these in S and h.
    RowDiff = RowBlock - RowStart_Block + 1
    TempBlocks = (RowDiff-1)*N_ColBlocks+1 : RowDiff*N_ColBlocks
```

```
    %*****************************************************
    %Create Dynamic Spectrum (BEFORE windowing)
    Spect = conj(Efield).*Efield;
    %Sum the spectrum over ColsPerBlock column-blocks for this row
    for n = 1:N_ColBlocks
        Spect_block = Spect(1+(n-1)*ColsPerBlock : n*ColsPerBlock, :);
        Spect_onerow(n,:) = sum(Spect_block,1);
    end

    %Add the row into the appropriate row-block
    S(TempBlocks,:) = S(TempBlocks,:) + Spect_onerow;

    %*****************************************************
    %If Specified, apply the FT filter to the E-field
    if ~isempty(FTfilter)
        Efield = Filter_FT.*Efield;
    end

    %FT the E-field over all frequencies for each spatial pixel, x
    if Pad == 'y'
        ft_Efield = fft(Efield, 2*N_f, 2);
    elseif Pad == 'n'
        ft_Efield = fft(Efield, [], 2);
    end

    %Calculate the impulse response at each spatial pixel of this row, x
    IR = conj(ft_Efield).*ft_Efield;
    %Sum IR over ColsPerBlock column-blocks for this row.
    for n = 1:N_ColBlocks
        IR_block = IR(1+(n-1)*ColsPerBlock : n*ColsPerBlock, :);
        IR_onerow(n,:) = sum(IR_block,1);
    end
    %Accumulate the averages from each row within one chunk
    h(TempBlocks,:) = h(TempBlocks,:) + IR_onerow;
    %*****************************************************

    ComputationTime = toc - Time
    Time = toc;
end
%**********************************************************************%
```

And for the B1737 data processing:

```
%%%%%%%%%%%%%%%%%%%%%%%% Last Updated: 15 Jan. 2007 %%%%%%%%%%%%%%%%%%%%%%%
%
%************************* HELP FILE INFORMATION *************************%
% [Delay, Varargout] = fn_PT_SingleInput( WAPP,ImageNum,DataInput )
%
% This is a function m-file that takes a data path (either Dynamic or
% Secondary spectrum) and calculates the delay for PSR B1737+13.
%
% Dependent function files:
%   - fn_mk_from_ObsDyn
%   - fn_ObsDyn_PlotRange
%   - fn_ObsSec_PlotRange
%   - fn_dBHistogramMode
%   - fn_FindLocByInterp
%*************************************************************************%


function [SecDelay,AcfDelay,varargout] = fn_PT_SingleInput(WAPP,...
                                                        ImageNum,DataInput)

%*********************** Import and Organize Data ***********************%
%Unpack DataInput
Pulsar = DataInput{1};
Num_f = DataInput{2};
Window = DataInput{3};
Zeropad = DataInput{4};
Zeromean = DataInput{5};
Dyn_tSize = DataInput{6};
Dyn_tShift = DataInput{7};
VisualCheck = DataInput{8};
SaveVisCheck = DataInput{9};
TrimScale = DataInput{10};
SaveDir = DataInput{11};
Color = DataInput{12};
Root = DataInput{13};
Aux = DataInput{14};
VisualAux = DataInput{15};
SaveVisAux = DataInput{16};
```

```
%Data path information
MJDlist_path = [Root,'MJDlist.txt'];
FREQlist_path = [Root,'FREQlist.txt'];
Directory = ['w',num2str(WAPP),'\'];

%Load the file list (specified by MJD of observation)
MJDlist = load('-ascii', MJDlist_path);
MJD = num2str(MJDlist(ImageNum));

%Load observational parameters
FREQlist = load('-ascii', FREQlist_path);
Freq = FREQlist(WAPP);                      %in MHz
BW = 50;                                    %in MHz
ChannelWidth = BW/Num_f;                    %in MHz
SamplingInterval = 10;                      %in seconds
MaxDelay = 1/(2*ChannelWidth);              %in microseconds
MaxFringeFreq = 1000/(2*SamplingInterval);  %in mHz



%select the file specified by ImageNum
DataPath = [Root,Directory,Pulsar,'.wapp',num2str(WAPP),'.',MJD,'.0.dyn.fit']
Dyn = fitsread(DataPath)';
[Num_f, Num_t] = size(Dyn)

%Begin the dynamic spectrum time-partition sequence
%Caclulate the total number of realizations possible
NumDyn = floor((1-Dyn_tSize)/Dyn_tShift)+1

for N = 1:NumDyn
    tRange = floor([(N-1)*Num_t*Dyn_tShift+1, ...
                   Num_t*((N-1)*Dyn_tShift + Dyn_tSize)]);
    DynChunk = Dyn(:, tRange(1):tRange(2));
    DynChunk = DynChunk/max(max(DynChunk));

    %Calculate the Secondary Spectrum with the specified options
    Output = fn_mk_from_ObsDyn(DynChunk,'sec','acf',{'Zeromean',Zeromean},...
                              {'Zeropad',Zeropad},{'Window',Window});
    sec = Output{1};
    acf = Output{2};
```

```
%Size of data
[Num_ff,Num_ft] = size(sec);

%Cut in half, shift, and scale the Secondary Spectrum
sec = sec(1:Num_ff/2,:); %This includes the unique central row
sec = fftshift(sec,2)/max(max(sec));
[Num_ff,Num_ft] = size(sec)

%Convert the Secondary Spectrum to a decibels scale
secdb = 10*log10(sec/max(max(sec)));
%*********************************************************************%


%************* Set Secondary Spectrum Processing Variables *************%
%Correct for central spike (y/n/m)
%(NOTE: 'm' checks to see if correction is needed)
Spike = 'm';
Width = 4;  %half the width of the spike in pixels
Tolerance = 10;
 %(NOTE: for Spike = 'm',
 %if P(spike) > Tolerance*BackgroundNoise, UseSpike = 'y')

%Size of "delay ~0 bias removal" samples
DelayFrac = 1/10;
FreqFrac = 1/5;

%Size of "background noise removal" samples (NOTE: for Mode = 1 only)
DelayFrac2 = (1-DelayFrac) - 5/Num_ff;
FreqFrac2 = 1/10;
%**********************************************************************%
toc


%********************** Noise Reduction Algorithm **********************%
%The dimensions of the bias and noise boxes in pixels
PixDelay = round(Num_ff*DelayFrac);
PixFreq = round(Num_ft*FreqFrac);
PixDelay2 = round(Num_ff*DelayFrac2);
PixFreq2 = round(Num_ft*FreqFrac2);
```

```
%%%%%%%Account for the Background Noise
%Background noise analysis mode
%   1 = Background Sample
%   2 = Histogram Mode

NoiseCalcMode = 2
if NoiseCalcMode == 1
    %The linear power of the mode of the dB (splined)
    %histogram is the background
    Method = 1;
    NumHistBins = (Num_ff + Num_ft)/2;
    Bins = linspace(min(min(secdb)),max(max(secdb)), NumHistBins);
    BackgroundNoise(NoiseCalcMode) = fn_dBHistogramMode(sec, Bins, Method);
elseif NoiseCalcMode == 2
    %The average of patch samples is the background
    Sample1 = sec(Num_ff-PixDelay2:Num_ff,1:PixFreq2);
    Sample2 = sec(Num_ff-PixDelay2:Num_ff,Num_ft-PixFreq2+1:Num_ft);
    Noise(1) = mean(mean(Sample1));
    Noise(2) = mean(mean(Sample2));
    BackgroundNoise(NoiseCalcMode) = mean(Noise);
end

%Subtract the background noise (preserve sec)
Sec = sec - BackgroundNoise(NoiseCalcMode);

%%%%%%%Remove the delay ~0 bias
%Find the mean intensity of each delay row within the bias boxes
MeanIntensity1 = mean(Sec(1:PixDelay,1:PixFreq), 2);
MeanIntensity2 = mean(Sec(1:PixDelay,Num_ft-PixFreq+1:Num_ft), 2);
MeanIntensity = (MeanIntensity1+MeanIntensity2)/2;

%Subtract the bias weight from each delay row
for n = 1:PixDelay
    Sec(n,:) = Sec(n,:) - MeanIntensity(n);
end

%%%%%%%Account for central spike in image (temporary solution)
Half_ft = round(Num_ft/2);
if Spike == 'y'
    Sec(PixDelay+5:Num_ff,Half_ft-Width:Half_ft+Width) = 0;
```

```
        UseSpike = 'y';
    elseif Spike == 'm'
        if mean(mean(sec(2*PixDelay+5:Num_ff,Half_ft-Width:Half_ft+Width)))
        > Tolerance*BackgroundNoise(NoiseCalcMode)
            Sec(PixDelay:Num_ff,Half_ft-Width:Half_ft+Width) = 0;
            UseSpike = 'y';
        else UseSpike = 'n';
        end
    elseif Spike == 'n'
        UseSpike = 'n';
    end
    %*************************************************************%


    %%%%%%%%%%%%%%%%% Find Delay from Secondary Spectrum %%%%%%%%%%%%%%%%
    %Sum of power at each index of delay (ACF of scattered pulse)
    Weight = sum(Sec,2);

    %Weight each index by the power at that delay
    Index = linspace(1,Num_ff,Num_ff)';
    WeightedIndex = Weight.*Index;

    %Caclulate the delay as a function of integration duration
    CumDelayIndex = cumsum(WeightedIndex)./cumsum(Weight);
    %Convert from delay indices to delay in microseconds
    CumDelay = (MaxDelay/(Num_ff-1))*(CumDelayIndex-1);

    %The Delay is the maximum element of CumDelay (INSTEAD of the last)
    [SecDelay(N), MaxLoc] = max(CumDelay);

    %%%%%%%%%%%%%%% Find Delay from Dynamic Spectrum ACF %%%%%%%%%%%%%%%%
    %Calculate the ACF of the Dynamic Spectrum from the PROCESSED sec,
    %retaining the unique central row when recreating the full secondary.
    FullSec(Num_ff+1:2*Num_ff,:) = Sec;
    FullSec(2:Num_ff,:) = fliplr(flipud(Sec(2:Num_ff,:)));
    Acf = ifft2(FullSec);
    Acf = sqrt(Acf.*conj(Acf));


    %Extract the zero time-lag column (for the diffractive bandwidth)
```

```
    Acf_t0 = Acf(:,1);
    %Interpolate to find the HWHM point of Acf_t0.
    InterpACF_HWHM = fn_FindLocByInterp(Acf_t0,'WHM');
    %Convert pixel number of HWHM into physical units (MHz)
    deltaF = (InterpACF_HWHM-1)*ChannelWidth;
    AcfDelay(N) = 1/(2*pi*deltaF); %in microseconds

    if Aux == 'y'
        %Extract the zero frequency-lag row (for the diffractive timescale)
        Acf_f0 = Acf(1,:);
        %Interpolate to find the 1/e point of Acf_f0.
        InterpACF_1oe = fn_FindLocByInterp(Acf_f0,'1/e');
        %Convert pixel number of 1/e point into physical units (seconds)
        deltaT(N) = (InterpACF_1oe-1)*SamplingInterval;
    end

    %%%%%%%%%%%%%%%%%%%%%%%%%%%%%%%%%%%%%%%%%%%%%%%%%%%%%%%%%%%%%%%%%%%%%%%
end

%If auxilliary information has been requestd, assign it to varargout
if Aux == 'y'
    varargout = {deltaT,deltaF};
end
```

Bibliography

[1] Hankins, T. H. & Rickett, B. J. Pulsar signal processing. In *Methods in Computational Physics Volume 14 — Radio Astronomy*, 55–129 (Academic Press, New York, 1975).

[2] Cordes, J. M., Rickett, B. J., Stinebring, D. R. & Coles, W. A. Theory of Parabolic Arcs in Interstellar Scintillation Spectra. *Astrophys. J.* **637**, 346–365 (2006). `astro-ph/0407072`.

[3] Stinebring, D. R. *et al.* Faint Scattering Around Pulsars: Probing the Interstellar Medium on Solar System Size Scales. *Astrophys. J., Lett.* **549**, L97–L100 (2001).

[4] Hill, A. S. *et al.* Deflection of Pulsar Signal Reveals Compact Structures in the Galaxy. *Astrophys. J., Lett.* **619**, L171–L174 (2005). `astro-ph/0411752`.

[5] Lyne, A. G. & Lorimer, D. R. High birth velocities of radio pulsars **369**, 127–129 (1994).

[6] Flanagan, É. É. & Hughes, S. A. The basics of gravitational wave theory. *New Journal of Physics* **7**, 204–+ (2005). `gr-qc/0501041`.

[7] Will, C. M. The Confrontation between General Relativity and Experiment. *Living Reviews in Relativity* **9**, 3–+ (2006). `gr-qc/0510072`.

[8] Stairs, I. H. Testing General Relativity with Pulsar Timing. *Living Reviews in Relativity* **6**, 5–+ (2003). `astro-ph/0307536`.

[9] Jaffe, A. H. & Backer, D. C. Gravitational waves probe the coalescence rate of massive black hole binaries. *Astrophys. J.* **583**, 616–631 (2003).

[10] Taylor, J. H. Pulsar timing and relativistic gravity **341**, 117–134 (1992).

[11] Jenet, F. A., Hobbs, G. B., Lee, K. J. & Manchester, R. N. Detecting the Stochastic Gravitational Wave Background Using Pulsar Timing. *Astrophys. J., Lett.* **625**, L123–L126 (2005).

[12] Cordes, J. M. Pulsar Observations I. — Propogation Effects, Searching, Distance Estimates, Scintillations and VLBI. In *ASP Conf. Ser. 278: Single-Dish Radio Astronomy: Techniques and Applications*, 227–250.

[13] Coles, W. A., Filice, J. P., Frehlich, R. G. & Yadlowsky, M. Simulation of wave propagation in three-dimensional random media. *App. Opt.* **34**, 2089–+ (1995).

[14] Lee, L. Wave propagation in a random medium: A complete set of the moment equations with different wavenumbers. *J. Math. Phys.* **15**, 1431–1435 (1974).

[15] Martin, J. M. & Flatte, S. M. Intensity images and statistics from numerical simulation of wave propagation in 3-D random media. *App. Opt.* **27**, 2111–2126 (1988).

[16] Gwinn, C. R. *et al.* Interstellar Optics. *Astrophys. J.* **505**, 928–940 (1998).

[17] Rickett, B. J. Amplitude-modulated noise - an empirical model for the radio radiation received from pulsars. *Astrophys. J.* **197**, 185–191 (1975).

[18] Löhmer, O., Mitra, D., Gupta, Y., Kramer, M. & Ahuja, A. The frequency evolution of interstellar pulse broadening from radio pulsars. *Astron. Astrophys.* **425**, 569–575 (2004). `astro-ph/0406601`.

[19] Cordes, J. M. & Rickett, B. J. Diffractive Interstellar Scintillation Timescales and Velocities. *Astrophys. J.* **507**, 846–860 (1998).

[20] Rickett, B. J., Coles, W. A. & Bourgois, G. Slow scintillation in the interstellar medium. *Astron. Astrophys.* **134**, 390–395 (1984).

[21] Rickett, B. J., Coles, W. A. & Markkanen, J. Interstellar Scintillation of Pulsar B0809+74. *Astrophys. J.* **533**, 304–319 (2000).

[22] Cordes, J. M. Space velocities of radio pulsars from interstellar scintillations. *Astrophys. J.* **311**, 183–196 (1986).

[23] McClure-Griffiths, N. M., Johnston, S., Stinebring, D. R. & Nicastro, L. Diffractive Scintillation of the Pulsar PSR B1259-63. *Astrophys. J., Lett.* **492**, L49+ (1998). `astro-ph/9711012`.

[24] Cordes, J. M., Weisberg, J. M. & Boriakoff, V. Small–scale electron density turbulence in the interstellar medium. *Astrophys. J.* **288**, 221–247 (1985).

[25] Lee, L. C. & Jokipii, J. R. Strong scintillations in astrophysics. II - A theory of temporal broadening of pulses. *Astrophys. J.* **201**, 532–543 (1975).

[26] Lee, L. C. & Jokipii, J. R. Strong scintillations in astrophysics. III - The fluctuations in intensity. *Astrophys. J.* **202**, 439–453 (1975).

[27] Rickett, B. J., Lyne, A. G. & Gupta, Y. Interstellar fringes from PSR B0834+06 **287**, 739–752 (1997).

[28] Rickett, B. J. Radio propagation through the turbulent interstellar plasma. *Annu. Rev. Astron. Astrophys.* **28**, 561–605 (1990).

[29] Rickett, B. J. What do scintillations tell us about the Ionized ISM? *Chin. J. Astron. Atrophys.* (2007). In press.

[30] Boldyrev, S. & Königl, A. Non-Gaussian Radio-Wave Scattering in the Interstellar Medium. *Astrophys. J.* **640**, 344–352 (2006). `astro-ph/0501527`.

[31] Walker, M. A., Melrose, D. B., Stinebring, D. R. & Zhang, C. M. Interpretation of parabolic arcs in pulsar secondary spectra. *Mon. Not. R. Astron. Soc.* **354**, 43–54 (2004). `astro-ph/0403587`.

[32] Stinebring, D. R., Hill, A. S. & Ransom, S. M. Scintillation Arcs and Binary Pulsars with an Application to PSR J0737-3039. In Rasio, F. A. & Stairs, I. H. (eds.) *ASP Conf. Ser. 328: Binary Radio Pulsars*, 349–+ (2005).

[33] Reeves, D. Honors thesis, Oberlin College (2003).

[34] Hill, A. Honors thesis, Oberlin College (2005).

[35] Hill, A. S., Stinebring, D. R., Barnor, H. A., Berwick, D. E. & Webber, A. B. Pulsar scintillation arcs. i. frequency dependence. *Astrophys. J.* **599**, 457–464 (2003).

[36] Hobbs, G. B., Edwards, R. T. & Manchester, R. N. TEMPO2, a new pulsar-timing package - I. An overview. *Mon. Not. R. Astron. Soc.* **369**, 655–672 (2006). `astro-ph/0603381`.

[37] Edwards, R. T., Hobbs, G. B. & Manchester, R. N. TEMPO2, a new pulsar timing package - II. The timing model and precision estimates. *Mon. Not. R. Astron. Soc.* **372**, 1549–1574 (2006). `astro-ph/0607664`.

[38] Jenet, F. A. *et al.* Upper Bounds on the Low-Frequency Stochastic Gravitational Wave Background from Pulsar Timing Observations: Current Limits and Future Prospects. *Astrophys. J.* **653**, 1571–1576 (2006). `astro-ph/0609013`.

[39] Wyithe, J. S. B. & Loeb, A. Low-Frequency Gravitational Waves from Massive Black Hole Binaries: Predictions for LISA and Pulsar Timing Arrays. *Astrophys. J.* **590**, 691–706 (2003).

[40] Foster, R. S. & Backer, D. C. Constructing a pulsar timing array. *Astrophys. J.* **361**, 300 (1990).

[41] Hotan, A. W., Bailes, M. & Ord, S. M. High-precision baseband timing of 15 millisecond pulsars. *Mon. Not. R. Astron. Soc.* **369**, 1502–1520 (2006).

[42] You, X. P. *et al.* Dispersion Measure Variations and their Effect on Precision Pulsar Timing. *ArXiv Astrophysics e-prints* (2007). `astro-ph/0702366`.

[43] Foster, R. S. & Cordes, J. M. Interstellar propagation effects and the precision of pulsar timing. *Astrophys. J.* **364**, 123–135 (1990).

[44] Stairs, I. H. Pulsar Observations II. — Coherent Dedispersion, Polarimetry and Timing. 251–269.

[45] Hankins, T. H. & Rajkowski, J. M. Wide bandwidth signal processor for removing dispersion distortion from pulsar radio signals. *Rev. Sci. Instrum.* **58**, 674 (1987).

[46] Hobbs, G., Lyne, A. G., Kramer, M., Martin, C. E. & Jordan, C. Long-term timing observations of 374 pulsars. *Mon. Not. R. Astron. Soc.* **353**, 1311–1344 (2004).

[47] Hu, W., Romani, R. W. & Stinebring, D. R. *Astrophys. J.* **366**, L33 (1991).

[48] Hemberger, D. A. & Stinebring, D. R. Scintillation & Pulsar Timing: Low-level noise from the Kolmogorov halo. *Chin. J. Astron. Atrophys.* (2007). In press.

[49] Cordes, J. M., Pidwerbetsky, A. & Lovelace, R. V. E. Refractive and diffractive scattering in the interstellar medium. *Astrophys. J.* **310**, 737 (1986).

[50] Coles, W. A. & Rickett, B. J. UCSD Simulation of Plane Wave Propagation (2005).

[51] Wikipedia. Fourier transform — wikipedia, the free encyclopedia (2007). URL `http://en.wikipedia.org/`. [Online; accessed 2007].

[52] Bracewell, R. N. *The Fourier Transform and Its Applications*. Electric and Electronical Engineering Series (McGraw-Hill, 1965), 2 edn. — Sig.: Bk68.

[53] Fejer, J. A. The Diffraction of Waves in Passing through an Irregular Refracting Medium. *Royal Society of London Proceedings Series A* **220**, 455–471 (1953).

[54] Lang, K. R. Interstellar scintillation of pulsar radiation. *Astrophys. J.* **164**, 249–264 (1971).

[55] Stinebring, D. R. Polarimetry of the millisecond pulsar **302**, 690–692 (1983).

[56] Manchester, R. N., Hobbs, G. B., Teoh, A. & Hobbs, M. The Australia Telescope National Facility Pulsar Catalogue. *Astron. J.* **129**, 1993–2006 (2005).

[57] Hobbs, G., Lyne, A. G., Kramer, M., Martin, C. E. & Jordan, C. Long-term timing observations of 374 pulsars **353**, 1311–1344 (2004).